The mean and turbulent flow structure of a weak hydraulic jump

S. K. Misra,[1,a)] J. T. Kirby,[1] M. Brocchini,[2] F. Veron,[3] M. Thomas,[4] and C. Kambhamettu[4]
[1]*Center for Applied Coastal Research, University of Delaware, Newark, Delaware 19716, USA*
[2]*Istituto di Idraulica e Infrastrutture, Universit Politecnica delle Marche, Via Brecce Bianche, 60131 Ancona, Italy*
[3]*Graduate College of Marine Studies, University of Delaware, Newark, Delaware 19716, USA*
[4]*Department of Computer and Information Science, University of Delaware, Newark, Delaware 19716, USA*

(Received 1 June 2007; accepted 16 January 2008; published online 12 March 2008)

The turbulent air–water interface and flow structure of a weak, turbulent hydraulic jump are analyzed in detail using particle image velocimetry measurements. The study is motivated by the need to understand the detailed dynamics of turbulence generated in steady spilling breakers and the relative importance of the reverse-flow and breaker shear layer regions with attention to their topology, mean flow, and turbulence structure. The intermittency factor derived from turbulent fluctuations of the air–water interface in the breaker region is found to fit theoretical distributions of turbulent interfaces well. A conditional averaging technique is used to calculate ensemble-averaged properties of the flow. The computed mean velocity field accurately satisfies mass conservation. A thin, curved shear layer oriented parallel to the surface is responsible for most of the turbulence production with the turbulence intensity decaying rapidly away from the toe of the breaker (location of largest surface curvature) with both increasing depth and downstream distance. The reverse-flow region, localized about the ensemble-averaged free surface, is characterized by a weak downslope mean flow and entrainment of water from below. The Reynolds shear stress is negative in the breaker shear layer, which shows that momentum diffuses upward into the shear layer from the flow underneath, and it is positive just below the mean surface indicating a downward flux of momentum from the reverse-flow region into the shear layer. The turbulence structure of the breaker shear layer resembles that of a mixing layer originating from the toe of the breaker, and the streamwise variations of the length scale and growth rate are found to be in good agreement with observed values in typical mixing layers. All evidence suggests that breaking is driven by a surface-parallel adverse pressure gradient and a streamwise flow deceleration at the toe of the breaker. Both effects force the shear layer to thicken rapidly, thereby inducing a sharp free surface curvature change at the toe. © *2008 American Institute of Physics*. [DOI: 10.1063/1.2856269]

I. INTRODUCTION

Turbulent hydraulic jumps have long been of interest to engineers as efficient energy dissipaters in the design of control structures. In attempts to clarify the details of the turbulence structure, many laboratory experiments have been performed with various techniques like hot-wire anemometry (e.g., Rouse *et al.*[1] and Resch and Leutheusser[2]) and laser Doppler anemometry (Long *et al.*[3]). Rouse *et al.*[1] showed that the air entrainment process, the momentum and energy transfer, and the energy dissipation are strongly dependent on inflow conditions. Cheaper and easier to use point measurement probes such as micro acoustic Doppler velocimeters have also been used by Liu *et al.*[4] However, the authors found that the signal quality deteriorated with increased noise levels near the free surface due to air entrainment and the turbulent fluctuations of the interface. Consequently, they were unable to obtain any information about the flow in the "roller" region or near the free surface. It is also doubtful whether an intrusive method is appropriate to measure the kinematics of a flow which is very sensitive to perturbations. Being single point measurement techniques, these at best provide a sparse picture of the flow field, and reconstructing a spatial map can only be done in an ensemble-averaged sense. Particle image velocimetry (PIV), on the other hand, is an established nonintrusive technique which provides accurate and detailed instantaneous spatial maps of a flow field comparable in accuracy to those obtained from laser Doppler velocimetry (LDV) measurements (Hyun *et al.*[5]). Hornung *et al.*[6] performed PIV experiments on traveling hydraulic jumps/bores with Froude number range of 2–6. Lennon and Hill[7] did PIV experiments analyzing undular jumps in the Froude number (Fr) range 1.4–3. Fully turbulent breaking jumps could not be generated at these low Froude numbers. The complete flow field could not be investigated even using a mosaic of ensemble-averaged spatial maps because the laser sheet access was blocked by optically opaque metal supports on the channel bottom. The free surface for the lower Froude number cases could not be measured by a wave gage since it disturbed the flow and caused the jump to move. Standard point gage and image processing techniques were used but with limited success. All the above studies, and numerous others that the authors are aware of, have either focused on undular jumps where some of the energy deficit across the jump is accounted for by the mean flux of wave

[a)]Presently at: Halcrow, 22 Cortlandt Street, New York, New York 10007.

energy being swept downstream, or fully turbulent jumps with $Fr > 1.5$.

Weak hydraulic jumps, on the other hand, are believed to provide a simplified description of the flow in spilling breakers in the inner surf-zone in a frame of reference moving with the broken wave. The similarity with weak hydraulic jumps is particularly true because of the low Froude number where the downstream-to-upstream depth ratio ($\xi \equiv h_1/h_0$; h_0, and h_1 are the upstream and downstream depths, respectively) is similar to that of typical inner surf-zone breakers. These jumps fall under the general category of steady spilling breakers such as those generated by submerged hydrofoils (Duncan[8] and Battjes and Sakai[9]) which are strictly "quasi-steady" because of experimentally observed oscillations of the breaking zone (Duncan[10] and Banner[11]). In the saturated breaking zone for irregular waves, both field (Thornton and Guza[12]) and laboratory (Ting[13]) measurements have shown that the wave height-to-water depth ratio, known as the breaker index, varies from 0.4 to about 0.7. For a bore or, equivalently, a hydraulic jump, this gives ξ varying from 1.2 to 1.35. Based on Belanger's equation [see Eq. (1)], the corresponding upstream Froude number (Fr) varies from 1.15 to 1.26. For such low Froude number turbulent jumps, the energy dissipation in the transition region from supercritical to subcritical flow comes primarily from turbulence generated by the shearing action of the flow, similar to spilling breakers and bores (Battjes[14]). The resulting flow in this breaker region is highly intermittent both in space and time and encompasses a wide range of temporal and spatial scales. This makes it a challenging flow to be investigated experimentally.

The most comprehensive study to date of low Froude number, weakly turbulent jumps with breaking is that of Svendsen *et al.*[15] (SVBK00 hereafter) based on LDV data collected by Bakunin[16] at several streamwise and vertical locations. The Froude numbers for the jumps analyzed are in the range 1.37–1.62. They found that, contrary to the traditionally simplified formulations for a hydraulic jump, the effects of vertically nonuniform velocities and nonhydrostatic pressure are important for mass and momentum conservation. Although a significant amount of the turbulent structure was mapped by vertical profiles of LDV data at several streamwise locations, simple analytical approximations and assumptions had to be made to calculate streamwise gradients of flow properties, or the gradients had to be neglected altogether (for example, in the calculation of vorticity, the streamwise gradient of the vertical velocity had to be neglected since it could not be estimated accurately). Little attention was focused on the intermittency of the surface and its influence on the flow structure. A single recirculating flow region was found, bounded from below by a dividing streamline (above which the net volume flux was zero) and from above by the mean surface. The peak values of the turbulence intensities and Reynolds shear stress were found to be at or below the bottom of the dividing streamline.

Peregrine and Svendsen[17] were perhaps the first to suggest a mixing-layer model describing the similarities in the flow structure between breakers, bores, and weak hydraulic jumps based on qualitative photographic visualizations of bubble tracers. They suggested that "the surface roller does not play a dominant role in the dynamics of the wave." The analogy with mixing layers is further supported qualitatively by the photographic evidence in Hoyt and Sellin[18] which was, however, based only on the structure of large scale eddies since the high polymer solution used to visualize the flow suppressed the smaller scale motions. The LDV measurements of Battjes and Sakai[9] for short wavelength breakers have shown that a self-similar wake is generated behind the breaker. An analogy between hydraulic jumps and plane turbulent wall jets has also been suggested by several authors (e.g., Rajaratnam[19] and Narayanan[20]). However, recently, Chanson and Brattberg[21] have shown that a quantitative comparison between the parameters of the two flows is significantly affected by the air entrainment. This short summary reveals that many questions are still open regarding the detailed turbulence structure and dissipative mechanisms of steady breakers, in particular, weak hydraulic jumps. What is the appropriate topological description for the reverse-flow region? How important are the effects of surface turbulence compared to the turbulence generated in the breaker shear layer? Can the breaker shear layer be classified as a mixing layer as is often assumed in theoretical models for breakers (Svendsen and Madsen,[22] Cointe and Tulin,[23] and Rhee and Stern[24])?

In this paper, a PIV laboratory experiment of a turbulent hydraulic jump of $Fr \sim 1.2$ and a depth ratio $\xi \sim 1.3$ is discussed in detail. In the next section, we describe the experimental setup and the flow parameters. Section III describes the characteristics of the turbulent air–water interface. Intermittency characteristics and toe oscillations are analyzed. The mean and turbulent flow structure are described in detail in Sec. IV with specific emphasis on the breaker shear layer and the reverse-flow region. Further discussion and conclusions are presented at the end of the paper.

II. EXPERIMENTAL SETUP

The experiment was performed in a recirculating Armfield S6 tilting flume that is 4.8 m long and 30 cm wide, with glass side walls (9 mm thick) and a solid opaque bottom, the same facility used to collect the data analyzed by SVBK00, even though no extensive attempts were made to replicate the exact flow geometry and conditions. Indeed, with the known sensitivity of the geometry and flow in hydraulic jumps to external perturbations such as bottom roughness, inflow velocity, prejump entrainment (Henderson[25]), it was extremely difficult to replicate the exact flow conditions. Water was pumped into the upstream end of the channel through a number of screens and flow straightening devices, after which it flowed past an undershot weir. The undershot weir was constructed from a plexiglass plate with a thickness of 1 cm, and was wedged in between the flume walls. A metal support fixed the plate to the side rails of the flume. The distance from the bottom of the flume to the bottom edge of the weir was controlled by a screw attached to the metal support. The lower end of the plate was machined in order to yield a sharp uniform edge on the upstream side to minimize lateral variations of the inflow. The gaps between the weir

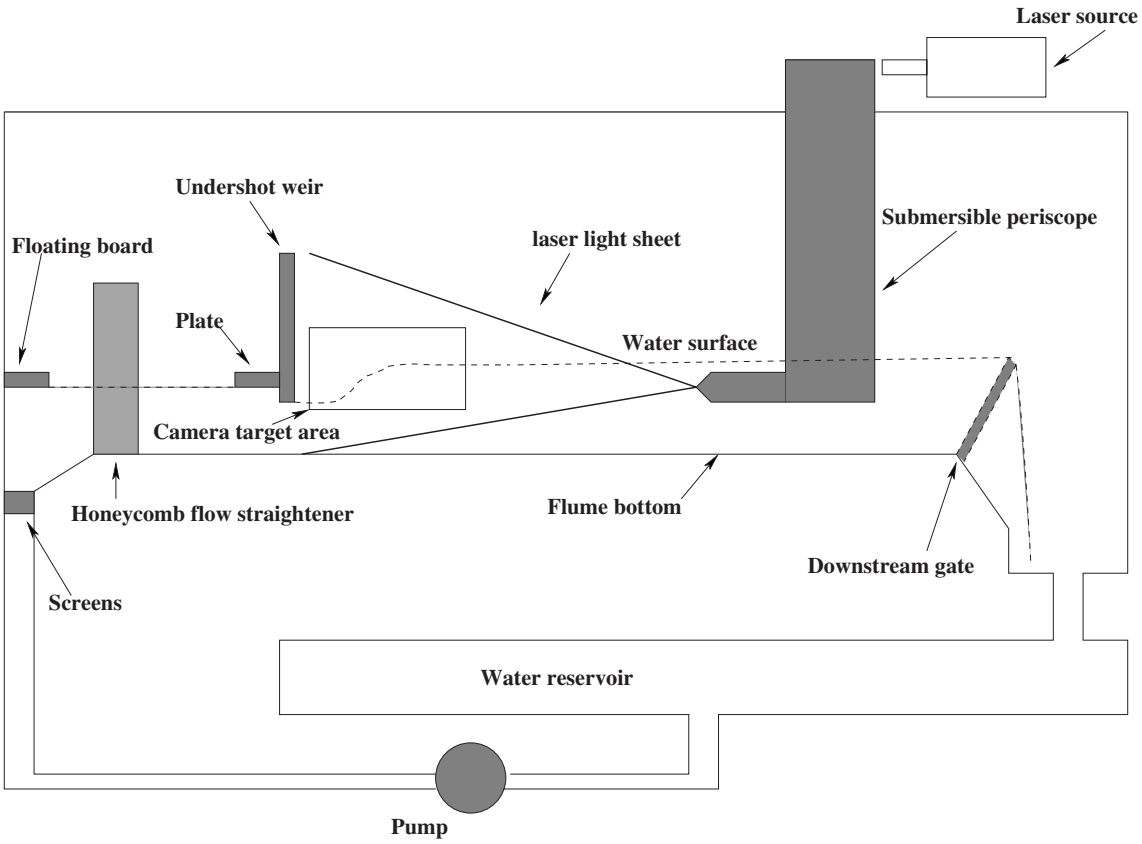

FIG. 1. Experimental setup.

and the side walls of the flume were made water tight by inserting flexible plastic tubes through grooves cut into the sides of the plate. The flow rate and the height of the weir were used to control the upstream flow velocity and water depth, thereby determining the upstream Froude number. Further downstream, the water flowed over the downstream gate (which was lowered or raised to fix the location of the jump) and into the reservoir. Just before the weir, the free surface was capped by a foam plate to damp out surface fluctuations on the upstream side. The flume was kept horizontal throughout the experiments. Figure 1 shows a schematic diagram of the flume and the PIV system configuration and Fig. 2 is a photograph of the jump. Figure 2 shows that cross-channel disturbances were negligible in the upstream part of the flow and reduced with increasing downstream distance from the breaker region. The jump did not have any visible undular characteristics. The jump characteristics are tabulated in Table I, where Q_m is the mean, vertically integrated volume flux.

The PIV setup consisted of a 120 mJ/pulse Nd-Yag new wave solo laser source with a pulse duration of 3–5 ns. This was mounted onto a custom-built submersible waterproof periscope which was lowered into the water. The optics were arranged in such a way that the laser beam emerged as a planar light sheet parallel to the flume wall. The laser sheet was aligned with the center plane of the flume away from the side wall boundary layers. Although the submersible was suitably streamlined, it changed the location of the jump and its position had to be adjusted so as to keep the jump stationary within the camera target area. It was kept far enough downstream of the jump to minimize flow interference and did not cause any visible changes to the flow. The flume bottom and the undershot weir were painted with water resistant black marine paint to minimize reflections from the laser sheet. As tabulated by Chow,[26] for painted, smooth steel surfaces, the Manning roughness coefficient is estimated to be 0.013. The water was seeded with 14 μm diameter silver coated hollow glass spheres with a specific gravity of 1.8 obtained from Potters Industries. From Maxey[27] and Wang

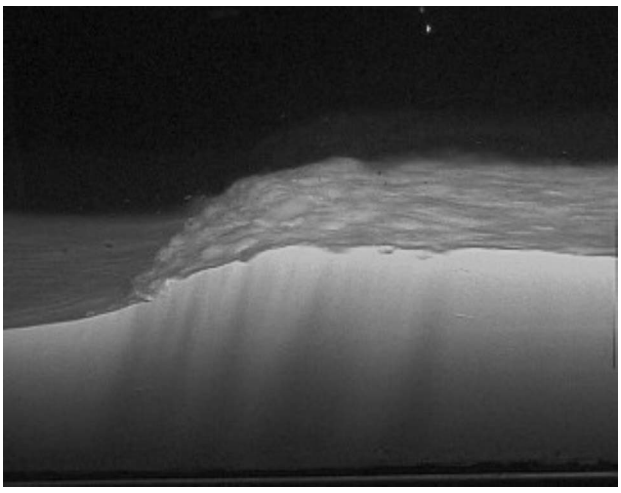

FIG. 2. Photograph of the hydraulic jump.

TABLE I. Jump parameters.

h_0 (cm)	h_1 (cm)	ξ	Q_m (l/s)	Fr
8.62	10.85	1.26	21.78	1.19

et al.,[28] the response time T_p of the particle is calculated to be $T_p = 1.96 \times 10^{-5}$ s. Flow time scales comparable to T_p, or larger, should be faithfully represented by the particles. A Kodak Megaplus 1.0 camera with a 1016 (vertical) $\times$1008 (horizontal) pixel CCD array with its image plane parallel to the flume wall, was used to visualize the flow. The target area dimensions were 23.3 cm (vertical) by 23.1 cm (horizontal). The distance of the CCD array from the laser sheet was 70.2 cm. The active area of the CCD sensor was 9.1 mm (horizontal) by 9.2 mm (vertical) and the fill factor was 55%. A 532 nm filter was used to reduce noise due to ambient light. A Dantec acquisition system was used to acquire the 8-bit gray scale images and store them onto a hard drive. The laser pulses were synchronized with the 30 Hz camera frame rate which ultimately led to a 15 Hz sampling rate for the instantaneous velocity fields. The time interval between two pulses in each image pair was 300 μs and each experimental run consisted of an ensemble of 1020 image pairs equivalent to 1020 instantaneous velocity maps.

III. THE AIR–WATER INTERFACE

There have been recent attempts to estimate air–water interfaces from PIV images with varying degrees of success (Hassan *et al.*,[29] Peirson,[30] Law *et al.*,[31] Lin and Perlin,[32] and Tsuei and Savaş,[33] among others). We have developed a robust and completely automated image processing algorithm to estimate the spatio-temporal evolution of the air–water interface for the present experiment. Only a brief description is given below. More details of the algorithm can be found in Misra *et al.*[34] and a recent application in Veron *et al.*[35] A raw PIV image, shown in Fig. 3, has four distinct regions. The coordinates are in pixels. The specularity seen in this particular raw image is from air bubble entrainment near the toe of the jump, due to breaking. Upon a careful visual analysis of the complete set of raw images, very few showed air bubbles resulting from prejump entrainment upstream of the sluice gate and minimal entrainment at the toe of the jump. The intersection of the laser light sheet with the bottom divides the lower region in the image into the fluid region and the solid flume bottom. This boundary is easily detected by standard edge detection techniques such as *Canny* or *Sobel* edge methods, and the result is shown as the dashed line. The black region at the top of the image is air and forms a sharp boundary from the rest of the image. This interface is also calculated by a *Canny* edge algorithm and is shown in the figure as the solid line. The diffuse region between this boundary and the actual surface (which should be the upper limit of the seeding particles) is due to the viewing angle of the camera which causes the water surface between the laser sheet and the flume wall to be reflected onto the image.

Using image segmentation methods, the air–water interface is calculated and is shown as the dotted line in Fig. 3. No attempt was made to resolve the small-scale surface undulations or account for the breakup of the surface due to breaking; a continuous, smooth contour was calculated to represent the interface. For two arbitrary images, the average absolute error across the whole domain was less than 6 pixels. The maximum error was found in the far upstream region where the elevation of the real surface was at times overpredicted because of the degradation of image content due to laser attenuation. The error was approximately 10 pixels or 2.3 mm (Misra *et al.*[34]). The overprediction of the actual surface leads to contamination of the near-surface velocities in the far upstream region and this is discussed further in the following. Due to the undulations in the water

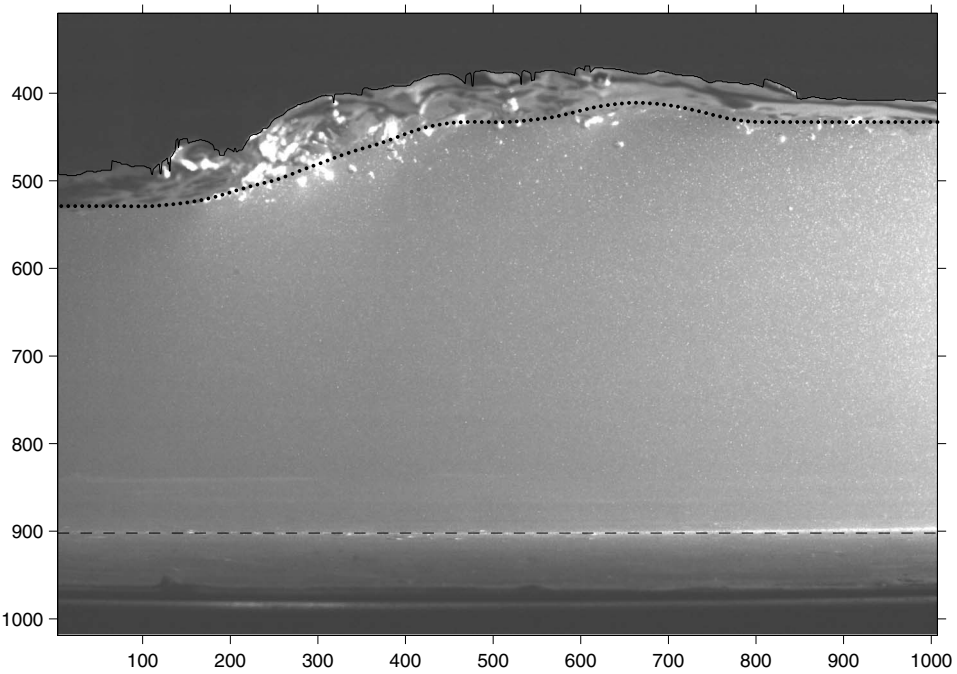

FIG. 3. Typical raw PIV image showing surface reflections and the interfaces: Flume bottom (dashed line), boundary between surface reflection region and air (solid line), and calculated actual free surface (dotted line).

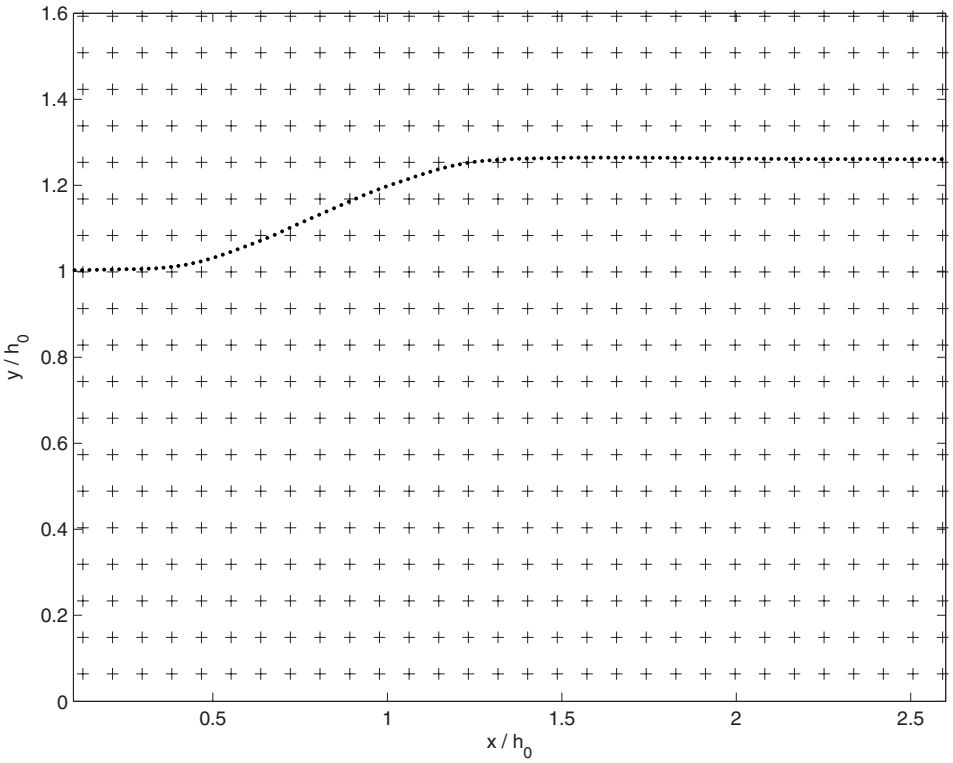

FIG. 4. Ensemble-averaged free surface (dotted line). The measurement grid is also shown at every fifth vertical and horizontal location.

surface between the laser light sheet and the sidewall, the camera line of sight can sometimes be blocked, leading to an underprediction of the interface. A quantification of such errors is not possible because of a lack of cross-channel measurements.

The vertical location of the Cartesian coordinate system (x,y) origin is defined at the flume bottom and the horizontal position at an arbitrary distance upstream of the mean toe location, similar to the coordinate system adopted by SVBK00. In SVBK00, the origin of the horizontal coordinate is placed at the mean position of the toe of the turbulent front and the mean position of the toe is, *a posteriori*, fixed at the beginning of the calculated roller geometry (see their Fig. 1). We believe it is more appropriate to define the toe location based on the surface curvature, and its estimation is discussed in detail in the following section. The supercritical and subcritical depths, taken here as the distances from the flume bottom to the end points of the ensemble-averaged free surface where the horizontal gradient of the surface was nearly zero, are found to be $h_0=8.62$ cm and $h_1=10.85$ cm, respectively, giving an upstream-to-downstream depth ratio $\xi=1.26$. The calculated values agree well with visually observed upstream and downstream depths. We note the difference in the definition of upstream depth with SVBK00 where it was fairly arbitrary and ambiguous because of the contraction immediately downstream of the sluice gate. Further, in SVBK00, the actual position where measurements were taken in front of the jump was somewhat arbitrary. In the present case, the toe of the jump was located further downstream of the sluice gate (approximately 20 cm; $>2h_0$) and multiple streamwise measurements were available upstream of the toe location. This led to, as shown in Fig. 4 (see also Fig. 2), a fairly spatially uniform upstream flow, and consequently, a more objective definition for the upstream depth.

From Belanger's equation,

$$\mathrm{Fr}=\sqrt{\frac{1}{2}\frac{h_1}{h_0}\left(\frac{h_1}{h_0}+1\right)}, \tag{1}$$

the upstream Froude number is calculated to be Fr=1.1932. Due to the error in the surface estimation, the upstream depth is slightly overpredicted and this leads to an underprediction of the Froude number of about 3%. The Froude number can also be determined based on a depth-averaged flow velocity or volume flux and is explored in the next section. It is perhaps surprising that we were able to obtain a breaking jump, which showed no visible undular characteristics, at such a low Froude number. The nature of the jump is very sensitive to the flow conditions and channel characteristics and it would require carefully designed control experiments to determine the specific cause(s) of breaking. Drastic qualitative and quantitative changes are known to occur in the nature of the jump through minor changes in the flow and channel characteristics, such as bottom roughness (Henderson[25]), inflow velocity profile (Resch and Leutheusser[2]), and prejump air entrainment (Chanson[36]). Chanson and Montes[37] have suggested that "the transition between an undular jump and a weak jump may occur for upstream Froude numbers in the range 1.0–3.6, the transition being a function of the upstream flow conditions."

A. Interface fluctuations and toe oscillation

For laboratory-generated steady spilling breakers, dominant coherent motions of the surface fluctuations and the breaker toe with peak frequencies in the range 0.47–3.75 Hz have been reported by various authors (Duncan[38]). In the

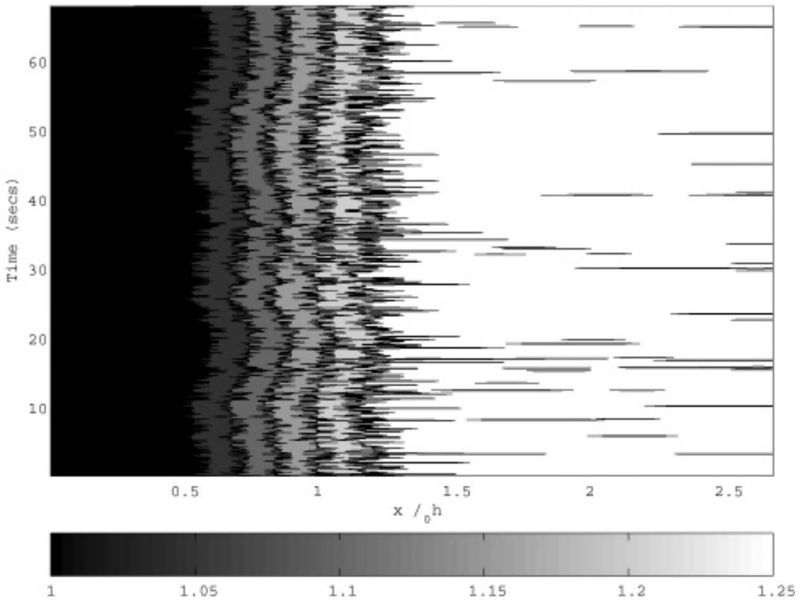

FIG. 5. Time stack of nondimensionalized surface profiles (η/h_0). The horizontal grayscale bar shows the magnitude of the nondimensional surface height. The five contours plotted, progressing from dark to light, are for $\eta/h_0=1.05$, 1.10, 1.15, 1.20, and 1.25.

present study, even though the sampling rate (15 Hz) is not high enough for capturing the smaller turbulent time scales, it is instructive to look at the unsteady nature of the fluctuations. Figure 5 shows a time stack of the dimensionless (with respect to h_0) surface profiles of the entire jump. The ensemble spans a total time of 67.93 s. The transitional breaking region shows coherent horizontal oscillations with a time scale of about 20 s or a frequency of 0.05 Hz. Since the length of the toe time series is small for a reliable Fourier spectral analysis and there are possible nonlinear effects in the signal, wavelet and Hilbert–Huang transforms (HHTs) were also used to compute the power spectrum of the time series in order to isolate the dominant frequency component. All three peaks were found to coincide at a frequency of approximately 0.05 Hz, which is the observed fluctuation frequency in the surface elevations. In order to determine the source of this slow oscillation, two Sontek Acoustic Doppler Velocimeters were placed near the inflow and outflow sections of the channel, 200 cm upstream of the sluice gate and 160 cm downstream of the toe. Time series of streamwise velocities were collected at 25 Hz, and spectral analyses showed a predominant peak at approximately 0.05 Hz at both locations. We believe that the long-time scale oscillation is intrinsic to the reservoir and pump system and unrelated to the turbulent dynamics at the toe of the breaker.

Tests with analytically constructed shear layer geometries showed that the contamination due to such a low frequency oscillation to the dynamics of the flow in the breaker shear layer is negligible. However, for increased confidence in the analysis, the effects of this oscillation were removed from both the raw computed interfaces and flow fields. From the ensemble of instantaneous interface realizations, we extracted time series of the horizontal oscillations at ten fixed elevations in the breaker region. These were then averaged and a fifth-order Butterworth low-pass filter with a cut-off frequency of 0.33 Hz was used to extract the low frequency oscillation. Both the averaged oscillations and the filtered time series are shown in Fig. 6. The maximum deviation caused by the oscillation is approximately equal to two measurement grid points. This filtered time series was then used to interpolate (using a bilinear interpolation) the interface and flow fields onto a common fixed grid at which the ensemble-averaged properties were calculated.

The toe itself is often loosely defined in the literature as noted by Duncan.[38] For incipient breaking of surface tension-dominated waves, the toe is defined as the leading edge of the bulge at the crest where the slope of the surface undergoes an abrupt change (Qiao and Duncan[39]). There is a sharp curvature at this point, and at a larger scale, the flow is marked by flow separation (Longuet-Higgins[40] and Duncan *et al.*[41]). For a fully evolved breaker, with a "roller" on the front face of the wave, the underlying turbulence and the significant corrugations of the surface make it difficult to precisely locate the toe. Banner[11] and Qiao and Duncan[39] have referred to the leading edge of the "roller" region as the toe. In saturated breakers or bores where the entire front face of the breaker is turbulent, Brocchini and Peregrine[42] have recently proposed a descriptive terminology of a "foot" as the base of the breaker, when looking down from above, with the fluctuations of the boundary between smooth and turbulent flow termed as "toes." In the present case, the air–water interface is approximated by a smooth unbroken curve. The toe is defined as the location of the maximum positive curvature of the free surface. The curvature (κ) of the instantaneous free surface (η) can be calculated as

$$\kappa = \frac{\dfrac{d^2\eta}{dx^2}}{\left[1+\dfrac{d\eta}{dx}^2\right]^{3/2}}. \tag{2}$$

Therefore, the toe motion in time can be tracked by computing the time series of the location of the peak curvature. An ensemble average of the locations of the maximum curvature calculated from the instantaneous surfaces is found to coin-

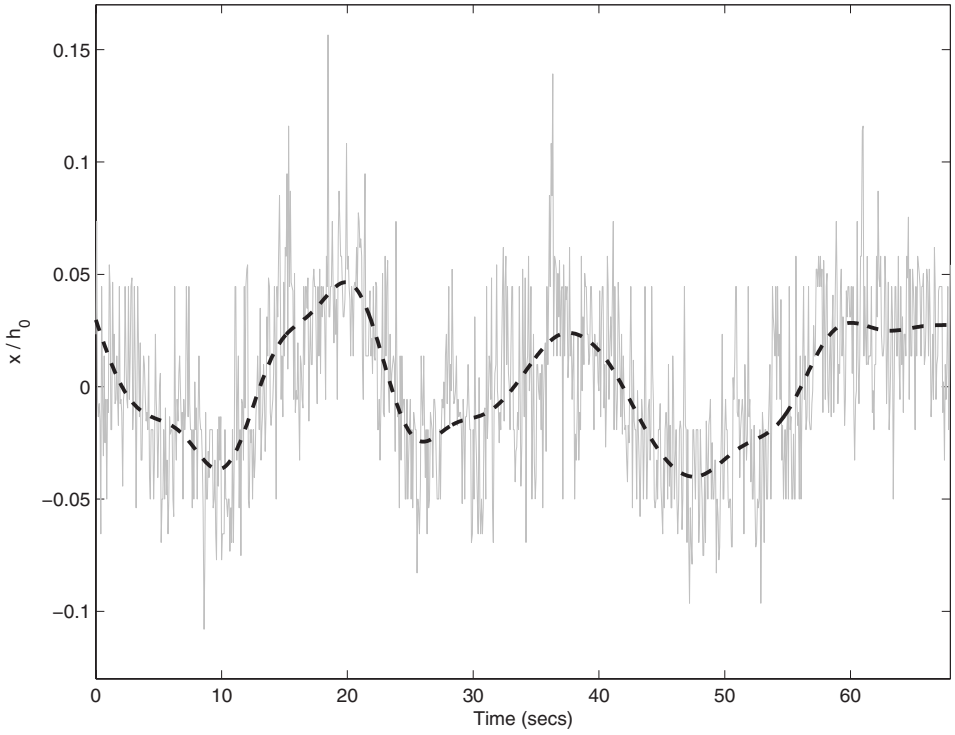

FIG. 6. Averaged surface oscillations in the breaker region (gray line) and low-pass filtered oscillation (dashed black line).

cide, within the measurement resolution, with the location of the maximum curvature of the ensemble averaged surface at $\tilde{x}=x/h_0\sim 0.47$ as shown in Fig. 7. The negative peak for the curvature is located at $\tilde{x}\sim 1.18$. The oscillatory nature of the curvature in the breaker region is linked to the surface estimation process with any small irregularities amplified by the second derivative in the curvature. These can easily be removed by manually drawing a smooth contour through the breaking region for the instantaneous images, but we do not think this is any more appropriate than that estimated by the algorithm since an air–water interface in this region cannot be defined unambiguously. Quantifying the numerical error associated with a second degree representation of the geometric curvature is extremely difficult, as, in addition to the numerical discretization error, the resolution in the horizontal direction (=8 pixels in our case) also comes into effect since

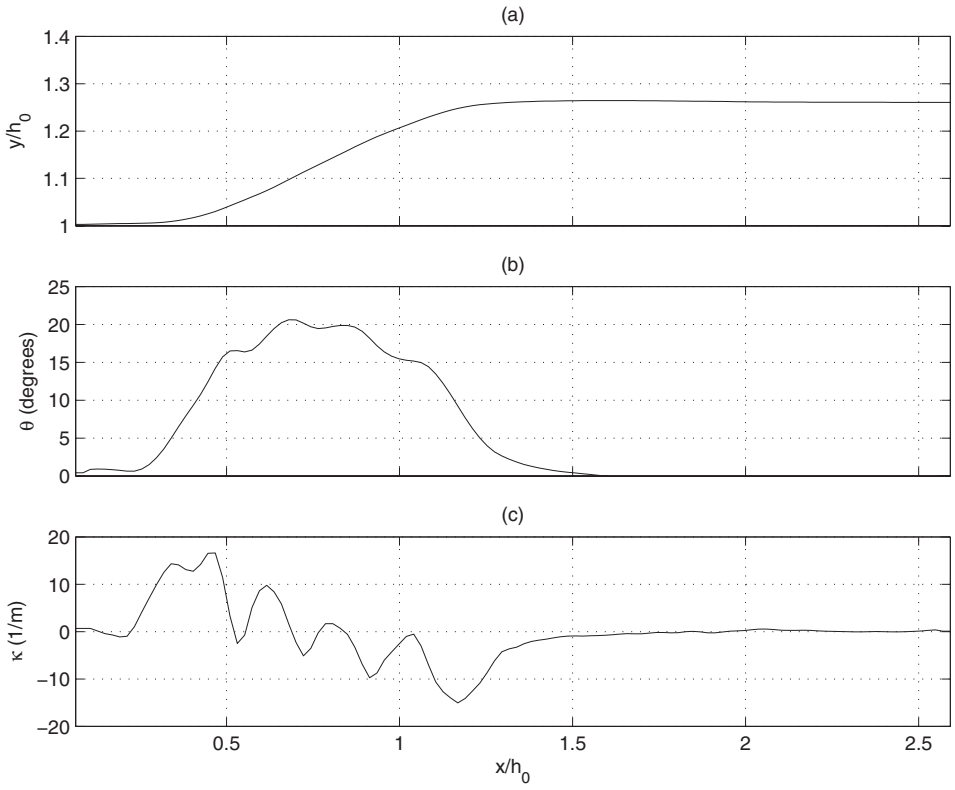

FIG. 7. (a) Ensemble-averaged free surface, (b) slope of the mean surface (degrees), and (c) curvature of mean surface.

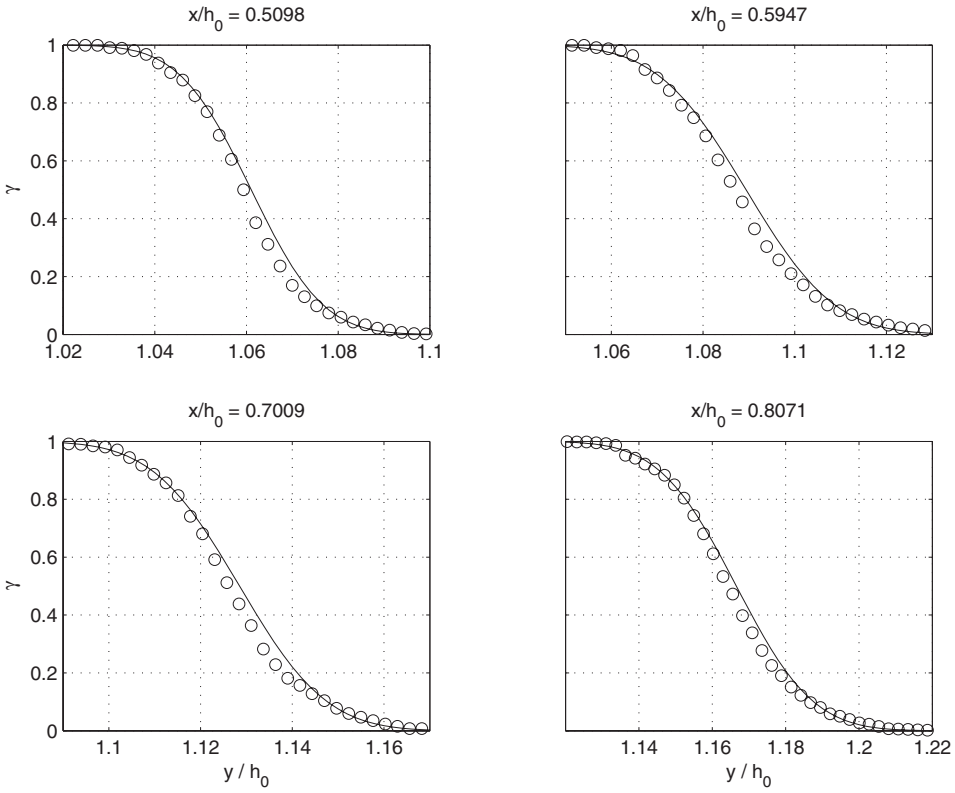

FIG. 8. Intermittency factor γ in the breaker region. Measured data (○) and theoretical error function (solid line).

we are primarily concerned with the horizontal location of the curvature peak. In similar experimental investigations, other authors such as Dabiri and Gharib[43] and Lin and Rockwell[44] have identified peaks in curvature by visual observation of the corrugations of the instantaneous surface, which itself was not directly measured, but either visually interpreted or estimated. In the present case, the slope of the mean surface shown in Fig. 7(b) at the location of the maximum curvature is found to be around 14°. This is close to the stable equilibrium value (10°–15°) typically used in the inner surf-zone for Boussinesq modeling of broken waves (Schäffer *et al.*[45] and Briganti *et al.*[46]) and is also in reasonable agreement with incipient breaking angles found by Salvesen and von Kerczek[47] and Duncan.[10] Longuet-Higgins[48] showed in a theoretical model of flow separation at a free surface that, immediately upstream of the toe, the free surface should be inclined to the horizontal at an angle lying between 10° and 20°.

B. Intermittency factor

It is essential to implement a conditional averaging technique for defining ensemble averages of the turbulent flow field for the intermittent reverse-flow region near the surface. Here, since the interface is assumed to be continuous and unbroken, separating the air and water phases, the intermittency arises from the fluctuation of the instantaneous surface. To deal with the interface intermittency, we apply a zone-averaging technique (Antonia[49]) obtained as the ensemble of values during times when a fixed measurement point is either in water or air. We define an intermittency function $I(x,y,i)$ at a spatial location (x,y) for the ith realization, as

$$I(x,y,i) = \begin{cases} 1, & \text{if } \eta(x,i) > y, \text{ i.e., if the point is in water} \\ 0, & \text{otherwise, i.e., if the point is in air,} \end{cases}$$

where $\eta(x,i)$ is the instantaneous water surface. The ensemble-averaged velocity thus becomes

$$\langle \mathbf{v} \rangle = \frac{\Sigma_{i=1}^{N} I\mathbf{v}}{\Sigma_{i=1}^{N} I}, \tag{3}$$

where N is the total number of realizations; $N=1020$. The zone-averaged intermittency factor $\gamma(x,y)$ is given by

$$\gamma = \frac{\Sigma_{i=1}^{N} I}{N}. \tag{4}$$

Corrsin and Kistler[50] have shown that the inferred distributions of turbulent interface fluctuations closely follow Gaussian error law distributions. A similar result was also observed at an air–water interface, on the basis of data of lower quality than that used here, by Killen and Anderson[51] and by Ervine and Falvey.[52] This illustrates that such similar behavior is a direct response of the interfaces (turbulent/laminar or air/water) to a random forcing (i.e., turbulence) as opposed to a deterministic one (i.e., waves). An illustration of this is also shown in Fig. 3 of Brocchini and Peregrine.[42] The present raw measurements have been shown to compare well to the error function profile at various locations inside the breaker region (see Fig. 10 in Misra *et al.*[34]). With the removal of the low-frequency oscillation, the comparison is significantly improved, as shown in Fig. 8. The Gaussian distribution of the surface fluctuations was further verified

from the observation that the ensemble-averaged free surface coincided with the contour of $\gamma=0.5$. Defining the location of the mean interface at $\gamma=0.5$ is an arbitrary choice which reflects a specific bias towards mass conservation arguments ($\gamma=0.5$ reflects equivalent phase volumes at that level). However, as shown by Brocchini and Peregrine,[53] for a simpler deterministic boundary like the shoreline, different mean interfaces can be found which match other conservation laws (e.g., flow-parallel momentum) and distinguishing which is the more dynamically important is rather subjective. Here, we simply note that measurements show that the ensemble-averaged air-water interface coincides with the location $\gamma=0.5$.

IV. FLOW STRUCTURE

A. The PIV algorithm

The PIV algorithm used here is described in detail in Thomas *et al.*[54] We have developed a phase-correlation based algorithm that first estimates the global motion field from a pair of PIV images and then uses this as an initialization for the local motion calculation. A pyramid hierarchy is used to percolate information from a coarse to fine resolution in a computationally efficient fashion. This helps achieve a very high spatial resolution without loss in accuracy (Nogueira *et al.*[55]). The velocity convergence at multiple spatial locations is found to be good and provides confidence in the final ensemble-averaged quantities. The motion estimation algorithm has been extensively tested for transient and nontransient strongly sheared flows such as the formation of a wake vortex, sensitivity to PIV image parameters, and reproduces accurate results when compared with ground-truth data with mean errors of $\pm 1\%$.

Once the real surface and bottom have been calculated, the raw image is cropped off at the location of the flume bottom and above the envelope of the highest surface fluctuations. The cropped image is then subdivided by finite windows of size 16×16 pixels with a 50% (8 pixels) overlap in the horizontal and vertical directions. The horizontal and vertical resolutions are, respectively, $\Delta x=\Delta y=0.184$ cm. In the vertical direction, the first calculation point is 8 pixels below the instantaneous surface, whereas the last calculation point is 16 pixels ($y_1=3.66$ mm) above the calculated bottom. These limitations were imposed by the size of the window used for computing the global motion (32×32 pixels). As noted before, all instantaneous raw velocity fields were mapped to a fixed grid using the extracted time series of the low frequency oscillation before ensemble-averaged quantities were calculated.

B. Mass flux conservation

The conditionally averaged mean velocities are calculated according to Eq. (3) and are represented hereafter as U and V in the x and y directions. Although there were no *in situ* measurements of the flow velocities, the accuracy of the computed flow field can be checked by examining an integral constraint based on mass flux conservation. The mean volume flux across a vertical section can be computed as

$$Q(x) = b\int_{y_1}^{h(x)} U(x,y)dy, \tag{5}$$

where b is the width of the channel, and the integration is done numerically. Note that the lower limit of integration is at y_1 and not the flume bottom. The contribution to the flux near the bottom, including the boundary layer, cannot be estimated because of lack of data. A comparison of the streamwise variation of the vertically integrated (to the mean surface) nondimensionalized volume fluxes between the present measurements, from $\tilde{x}\sim 0.47$, the toe location, to $\tilde{x}\sim 2.48$, and the Fr=1.46 case considered by SVBK00 is shown in Fig. 9. The standard deviation (Q_σ) and mean (Q_m) for the present measurements, from $\tilde{x}\sim 0.47$ to $\tilde{x}\sim 2.48$, are 0.5198 l/s and 21.784 l/s, respectively, which gives $Q_\sigma/Q_m=0.0239$. For the data analyzed in SVBK00, from the toe location to $\tilde{x}\sim 4.0$, $Q_\sigma/Q_m=0.0221$, which shows that volume fluxes calculated from the raw data for the two studies are comparably accurate. The effects of the bottom and sidewall boundary layers are not included in the volume flux estimate. By fitting analytic velocity profiles to the raw data and incorporating the non-negligible reductions in the total volume flux due to sidewall and bottom boundary layers, SVBK00 found that the streamwise deviations of the volume flux could be reduced further.

The Froude number can be calculated from the volume flux as

$$\mathrm{Fr}' = \frac{Q_m}{(bh_0')\sqrt{gh_0'}}, \tag{6}$$

where $h_0'=h_0-y_1$. The upstream Froude number is thus calculated to be $\mathrm{Fr}'=1.023$ which is smaller than Fr calculated from Eq. (1). This is in agreement with SVBK00 who found that the Froude number calculated from Belanger's equation consistently overpredicted a depth-averaged velocity or volume flux based estimate.

C. Mean flow structure

Figure 10 shows the vertical profiles of the mean horizontal velocity at $\tilde{x}=0.15$ and $\tilde{x}=2.50$. The dashed line is the elevation of the mean free surface at this location. As noted before, due to the overprediction of the height of the instantaneous surface in the far upstream region, the errors in the velocity at the measurement location just below the surface results in contamination of the shear layer near the surface shown in Fig. 10(a). The location of the velocity profile shown in Fig. 10(a) is further upstream of the toe than measurements reported in SVBK00 and a direct comparison cannot be made. As noted earlier, the jump location in the present case was further downstream of the sluice gate than in SVBK00. It is well established that the hydraulic jump location and the boundary layer structure are interdependent (Wilson and Turner[56]) and that the flow characteristics, particularly near the toe and the free surface, depend significantly on the inflow characteristics. The present measurements show that the bottom boundary layer at the toe location was more developed than was the case in SVBK00. At the downstream location shown in the right panel in Fig.

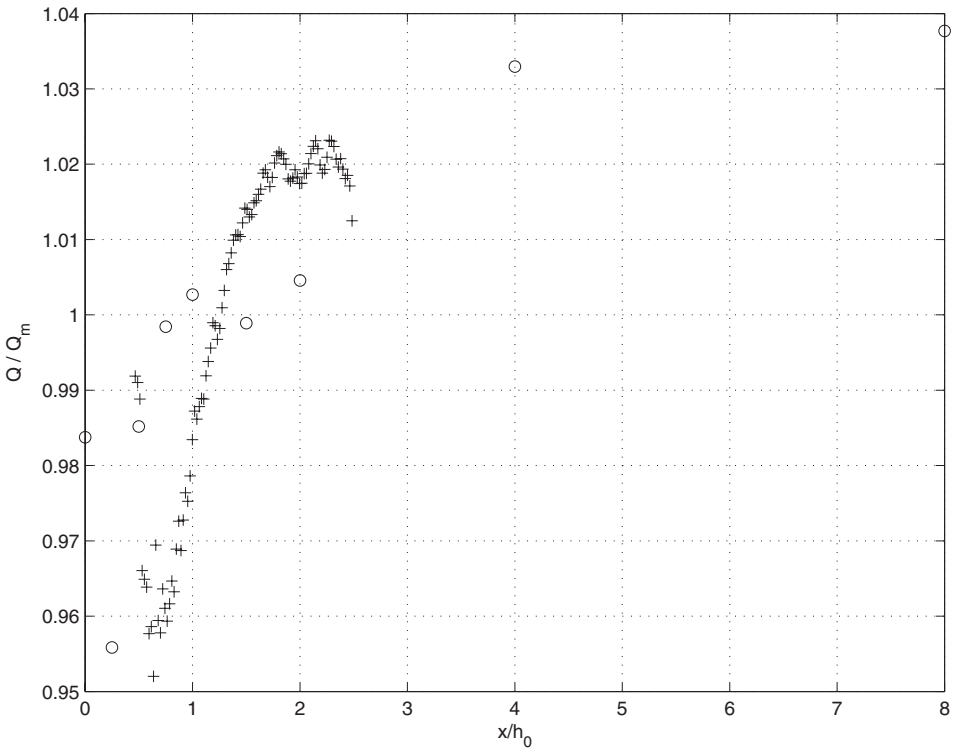

FIG. 9. Nondimensionalized vertically integrated volume flux. Raw data analyzed in SVBK00 (○) and present measurements (+).

10(b), the thickness of the shear layer is approximately 3 cm, showing that the flow has not relaxed to its depth-uniform open channel configuration. The velocity estimates at locations downstream of the toe are accurate up to the mean surface. For downstream flow conditions, Fig. 10(b) is very similar to that reported by SVBK00 (see their Fig. 2).

Next, we examine contour plots which present the whole spatial map of the flow field. In Fig. 11, the dotted line is the ensemble-averaged free surface. The flow fields are shown only up to the mean surface. The flow structure in the intermittent region is analyzed later. Although the mean horizontal velocities are nearly uniform around mid-depth, there are

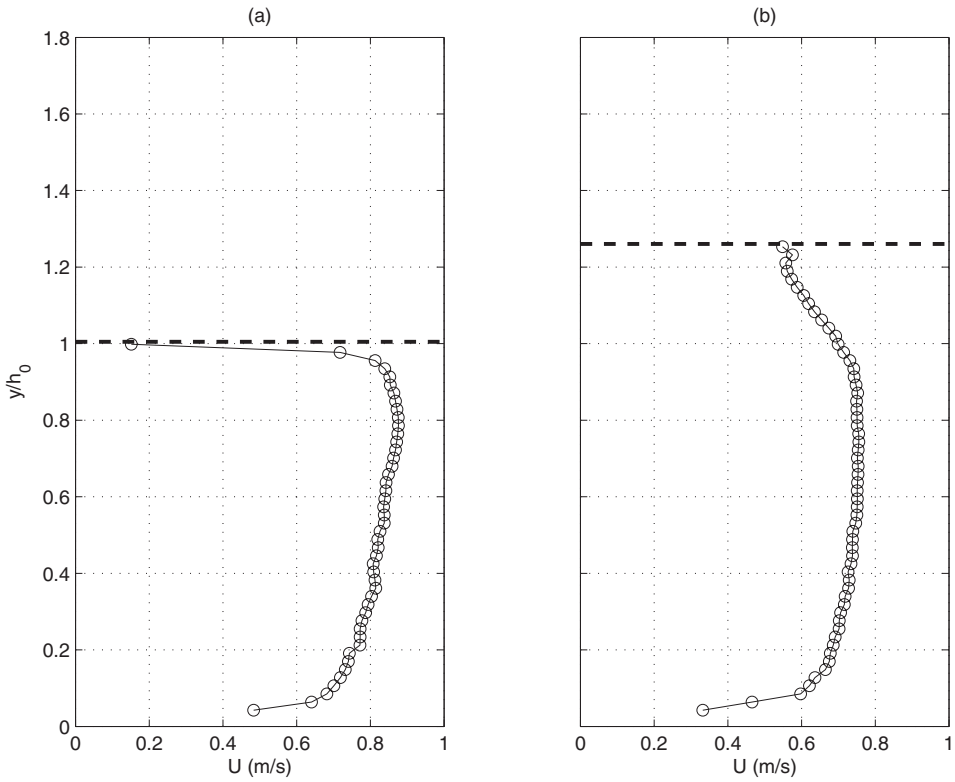

FIG. 10. Vertical profiles of the ensemble-averaged horizontal velocity U (m/s). (a) $\tilde{x}=0.15$, (b) $\tilde{x}=2.50$. The dashed lines show the location of the mean free surface.

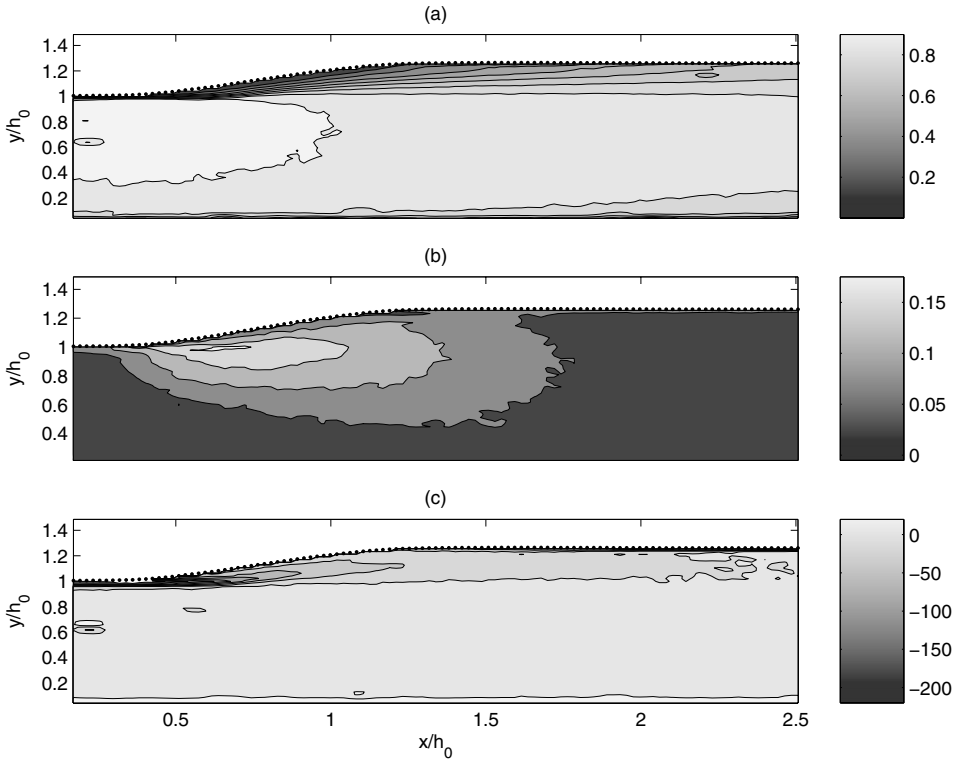

FIG. 11. Mean flow structure. (a) Ensemble-averaged horizontal velocity U (m/s), (b) ensemble-averaged vertical velocity V (m/s), and (c) ensemble-averaged vorticity ω (1/s) (detail shown in Fig. 12). The dotted line is the ensemble-averaged free surface. The toe of the breaker is at $\tilde{x} \sim 0.47$.

significant deviations from the assumption of depth-uniform flow, particularly in the breaker shear layer. The bottom boundary layer with positive vorticity also grows in the downstream direction. The vertical velocity is almost an order of magnitude smaller than the horizontal velocity and reaches its peak value, 0.2 m/s, downstream of the toe at $\tilde{x} \sim 0.68$, $\tilde{y} \sim 0.99$.

There is a thin, concentrated region of negative vorticity

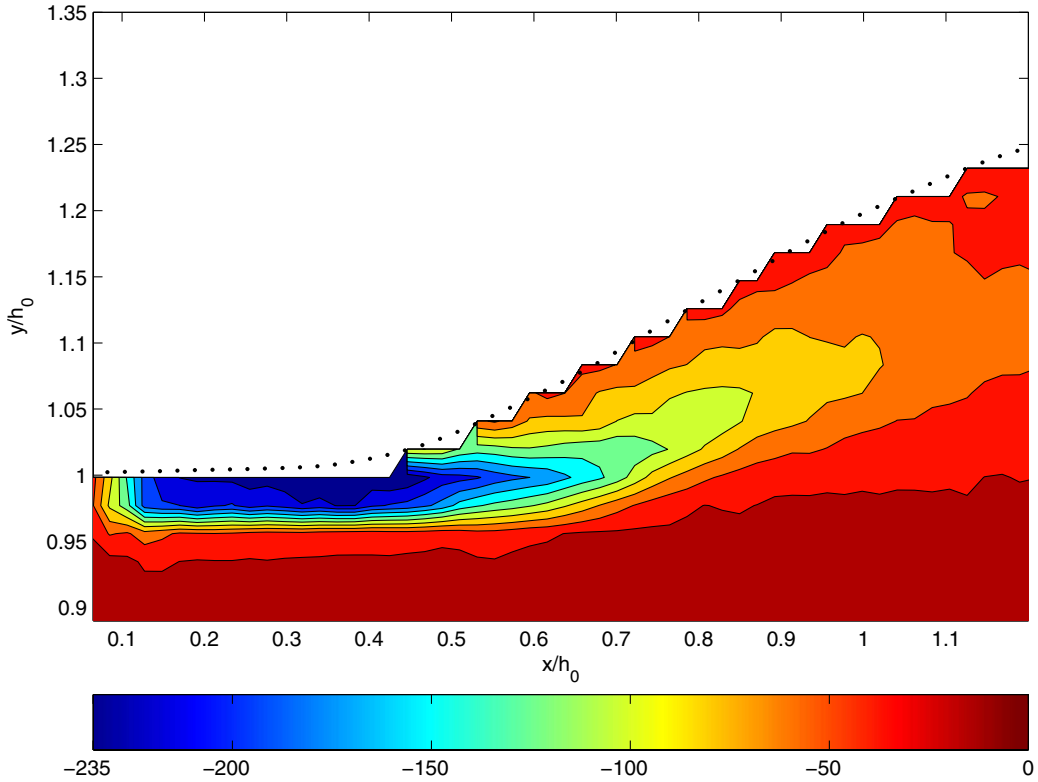

FIG. 12. (Color online) Ensemble-averaged vorticity (1/s). The dotted line is the mean free surface. The toe of the breaker is at $x/h_0 \sim 0.47$.

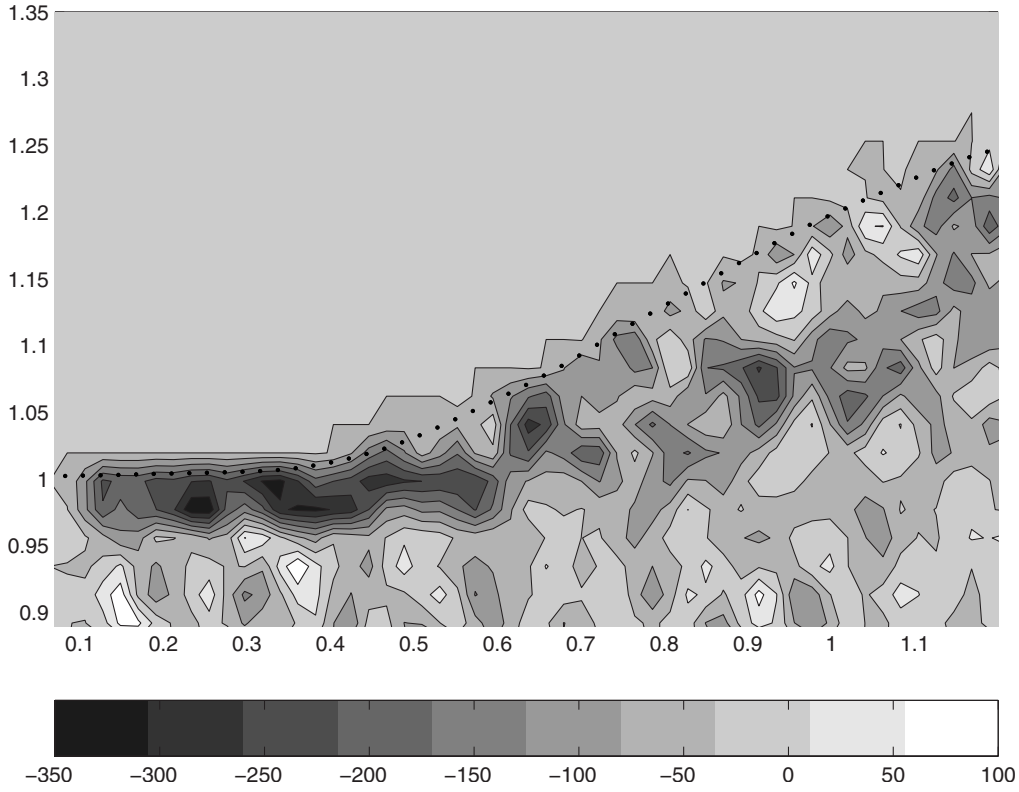

FIG. 13. Instantaneous vorticity (1/s). The dotted line is the mean free surface. The toe of the breaker is at $x/h_0 \sim 0.47$.

in the breaker shear layer (a special mixing layer whose features are discussed in detail in Sec. IV E 2), shown in more detail in Fig. 12. Near the toe, the negative vorticity decays rapidly away from the mean surface reaching 1% of its peak value at a distance of approximately 2.2 cm. Therefore, the bulk of the flow can be modeled as irrotational. In SVBK00, the vanishing vorticity at the mean surface was a consequence of the imposed zero mean shear stress condition for the analytic fit to the horizontal velocity. In the present study, we find a nonzero vorticity at the mean surface. As shown in Fig. 12, the mean vorticity has its peak, negative value upstream of the toe, at $\tilde{x} \sim 0.42$, $\tilde{y} \sim 0.99$, and decreases in the downstream direction. With the extent of available data, it is also clear that the vorticity decays to zero in the upstream streamwise direction as there cannot be any physical vorticity in the far upstream region away from the jump. The instantaneous vorticity is shown in Fig. 13. The streamwise variations of the instantaneous vorticity show well defined peaks, indicating coherent vortical motions in the shear layer. This is consistent with the observations made by Hornung *et al.*[6] during the initial stages of bore formation (see their Figs. 10 and 11). For detailed experimental observations on the vorticity generation mechanisms in steady breakers with respect to the free surface geometry, see Lin and Rockwell[44] and Dabiri and Gharib.[43]

The flow deceleration due to the convective term, $\hat{U}_s \partial \hat{U}_s / \partial s$, is shown in Fig. 14. This is computed on the basis of locally orthogonal, curvilinear coordinates (s,n) fixed on the mean surface (Brocchini and Peregrine[42]). s and n are measured along the surface parallel and normal directions, respectively. The mean surface-parallel and surface-normal velocities are, respectively, calculated as

$$\hat{U}_s = U \cos\theta + V \sin\theta \tag{7}$$

and

$$\hat{V}_n = -U \sin\theta + V \cos\theta. \tag{8}$$

$\theta(x) = \tan^{-1}[\partial \langle \eta(x) \rangle / \partial x]$ is the angle that the tangent to the mean surface makes with the x-axis, shown in Fig. 7(b). Since θ is determined from the local slope of the mean surface, the transformation is accurate only near the mean surface where the streamlines closely follow the surface. The surface-normal and surface-parallel gradients are therefore only shown until five measurement points below the mean surface. Although the peak negative value of the surface-parallel convective acceleration occurs at $\tilde{x} \sim 0.49$, $\tilde{y} \sim 0.98$ which is coincident within the measurement resolution with the toe location, intense flow deceleration is seen to occur upstream of the peak vorticity location. The localization of the deceleration, indicative of the strong reduction in velocity over a small streamwise distance, is in good agreement with the observations of Lin and Rockwell.[44]

Next, the flow in the intermittent region is analyzed. Figure 15 shows the mean surface-parallel $(\hat{U}_s)$ and surface-normal $(\hat{V}_n)$ velocities near the free surface, which, due to the curvature of the streamlines, are more appropriate in understanding the dynamics of the flow in this region, com-

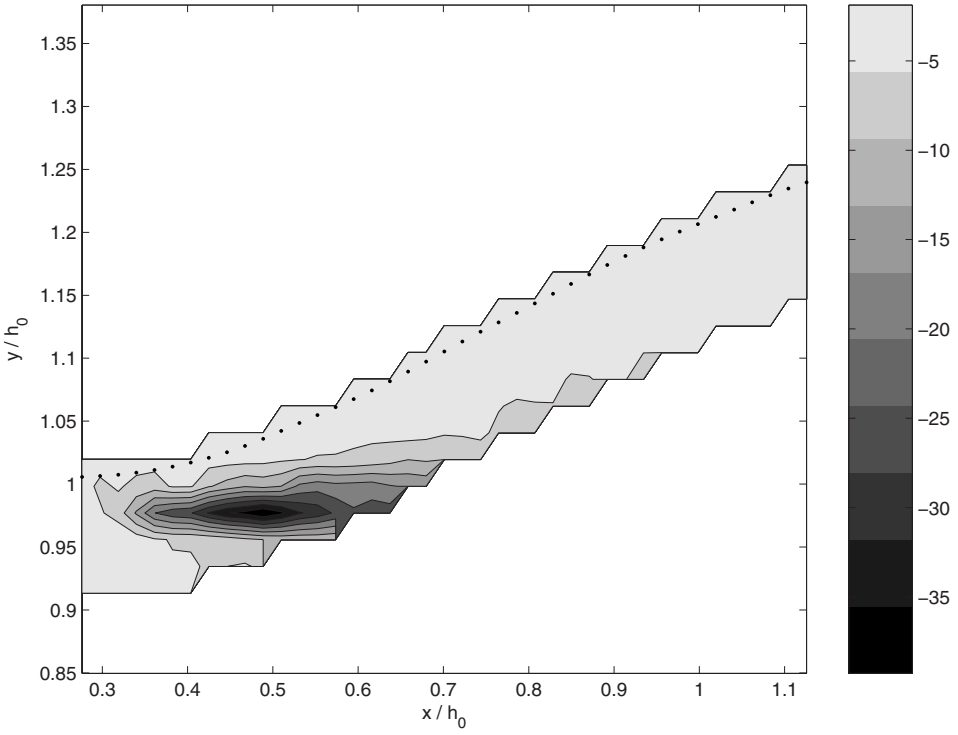

FIG. 14. Ensemble-averaged surface-parallel convective acceleration $\hat{U}_s \partial \hat{U}_s / \partial s$ $(\mathrm{m/s^2})$. The toe of the breaker is at $x/h_0 \sim 0.47$.

pared to the Cartesian forms presented in SVBK00. The dotted line is the mean surface. A weak reverse flow with the largest negative velocity found to be 2.38 cm/s is clearly seen and is localized entirely above the mean surface. SVBK00 determines the location of the lower boundary of a recirculating region by calculating the elevation below which the depth-integrated volume flux (obtained from an analytic fit to the measured velocities) goes to zero. This is in no way a trivial calculation. In the present case, we do not have enough vertical resolution in the very thin reverse-flow region to accurately estimate the volume flux. However, to conceptualize a recirculating region, the bottom boundary can be estimated by assuming that the positive velocities at the bottom boundary should be approximately equal to the maximum negative velocity in the reverse-flow region. Therefore, the bottom boundary should be just below the mean surface. This is a different scenario than SVBK00 where the entire recirculating region was confined below the

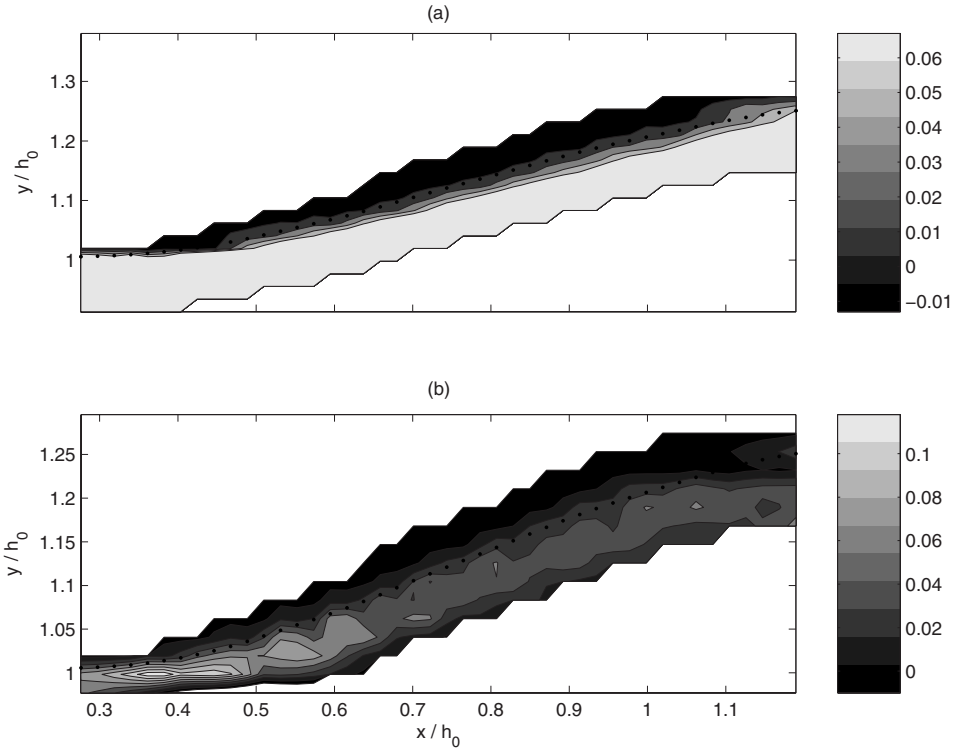

FIG. 15. (a) Mean surface-parallel velocity $\hat{U}_s$ (m/s) and (b) mean surface-normal velocity $\hat{V}_n$ (m/s). Dotted line is the ensemble-averaged free surface.

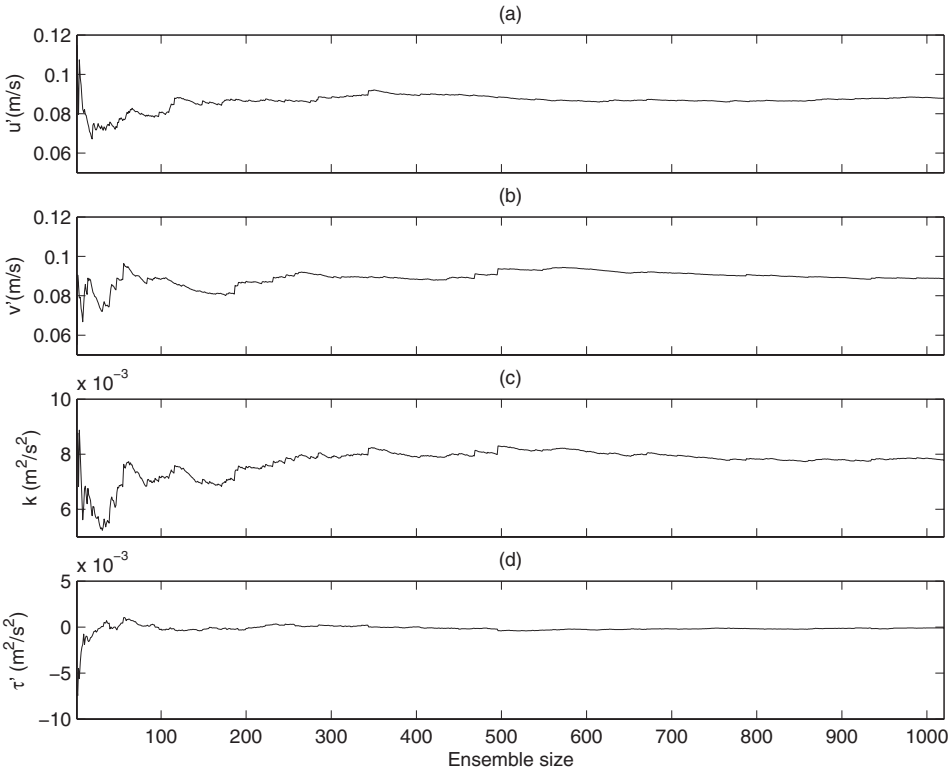

FIG. 16. Convergence of turbulence statistics at $\tilde{x}\sim 0.53$, $\tilde{y}\sim 0.96$. (a) Horizontal turbulent velocity u' (m/s), (b) vertical turbulent velocity v' (m/s), (c) turbulent kinetic energy k (m^2/s^2), and (d) Reynolds shear stress τ' (m^2/s^2).

mean surface. Since no velocity measurements were available above the mean surface in SVBK00, it is clear that the difference arises because of the treatment of intermittency in the present case.

The surface-normal velocity is nearly zero in the reverse-flow region. However, there are large, positive values of $\hat{V}_n$ below the mean surface and are an indication of the entrainment of fluid from below. This is in agreement with the conceptual "starting plume" model of Longuet-Higgins and Turner[57] (see their Fig. 7) where the spilling region is regarded as a turbulent gravity current riding down the front face of a wave, with entrainment of fluid from below. It is also clear from the present data that, though most of the entrainment occurs near the toe, inflow from below occurs all over the reverse-flow region. Note that the small-scale structure seen in the vertical velocity is resolved by the measurement location grid ($\Delta\tilde{x}=\Delta\tilde{y}=0.0213$; see Fig. 4 for measurement grid) and is not merely an artifact of the contour plotting routine. As opposed to the assumption made by SVBK00, the mean shear is finite and negative at the mean surface. Lastly, regarding the geometry of the reverse-flow region, the mean inclination is calculated to be 18°, which is close to the value ($\sim$17°) that have been found for steady breakers generated by submerged hydrofoils (Duncan[10] and Walker *et al.*[58]).

D. Convergence of turbulent quantities

The horizontal root mean square turbulent velocity is computed as

$$u' = \sqrt{\frac{\Sigma_{i=1}^{N}[I(u-U)]^2}{N\gamma}} \tag{9}$$

and similarly for v'. u and v are the instantaneous horizontal and vertical velocities, respectively. The turbulent kinetic energy (k) and Reynolds shear stress (τ') are computed as

$$k = \frac{\Sigma_{i=1}^{N} I\frac{1}{2}[(u-U)^2+(v-V)^2]}{\gamma N} \tag{10}$$

and

$$\tau' = -\frac{\Sigma_{i=1}^{N} I(u-U)(v-V)}{\gamma N}. \tag{11}$$

The convergence of turbulent quantities of interest is examined at a number of spatial locations prior to analyzing the turbulence structure of the flow field. This is performed by calculating running averages of the turbulence statistics over the entire ensemble. The convergence rates for the turbulent statistics are shown in Figs. 16 and 17. The horizontal coordinate is shown in terms of the ensemble size, since this illustrates the size of the ensemble needed to achieve satisfactory convergence, which is often an issue in PIV investigations of root mean square turbulent quantities (Ullum *et al.*[59]). In Fig. 16, convergence rates at a location in the breaker shear layer near the toe of the breaker at $\tilde{x}=0.53$, $\tilde{y}=0.96$ are shown. Figure 17 shows similar convergence statistics at $\tilde{x}\sim 1.0$ and $\tilde{y}\sim 1.1$, further downstream of the toe location, and as can be seen, satisfactory convergence is

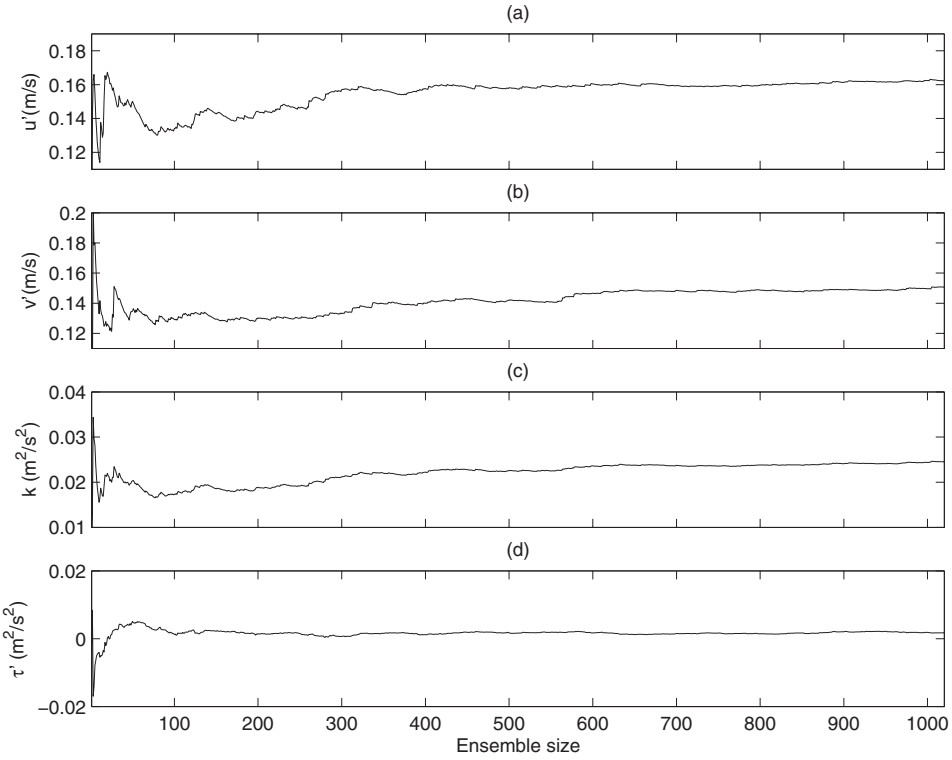

FIG. 17. Convergence of turbulence statistics at $\tilde{x}\sim 1.0$, $\tilde{y}\sim 1.1$. (a) Horizontal turbulent velocity u' (m/s), (b) vertical turbulent velocity v' (m/s), (c) turbulent kinetic energy k (m^2/s^2), and (d) Reynolds shear stress τ' (m^2/s^2).

attained faster. The convergence of the mean quantities are, everywhere, much faster than that of the turbulent quantities.

E. Turbulence structure

Figure 18 shows the spatial structure of the strongly nonisotropic turbulence of the breaker shear layer. Only a subsection of the entire domain is shown here for more detail and clarity. As expected, the turbulence intensity decays rapidly over depth outside the breaker shear layer. The horizontal and vertical root mean square turbulent velocities in the shear layer are of the same order as the mean velocities, with u' being slightly larger than v'. The peak value for the horizontal turbulence intensity is found at the toe. This is different from the measurements of Lennon and Hill[7] who had

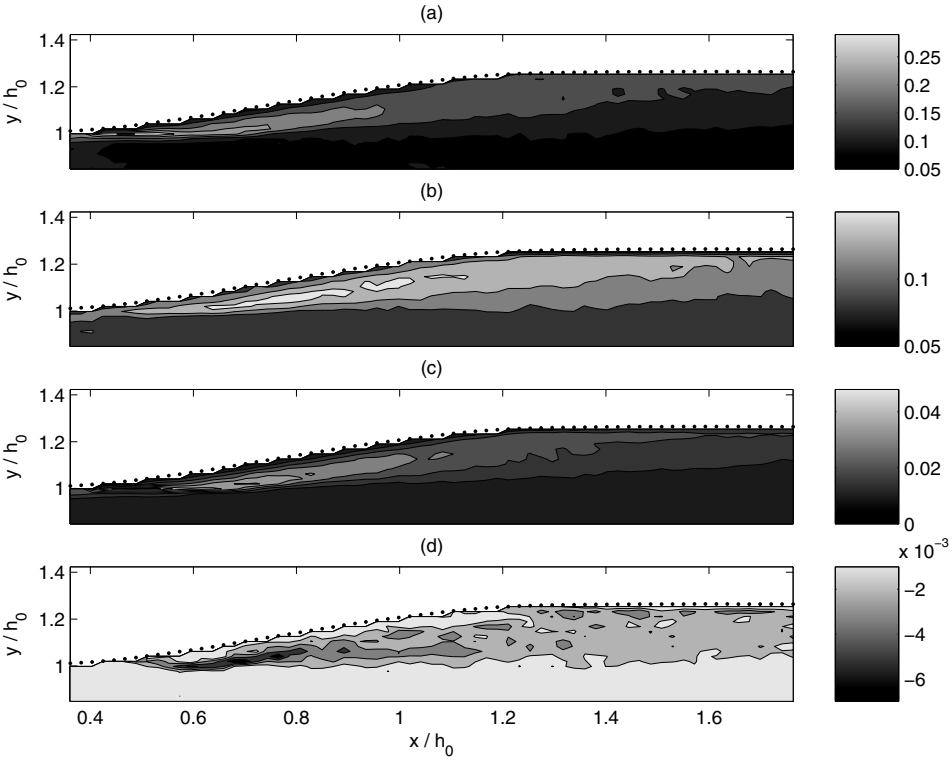

FIG. 18. Turbulence structure. (a) Horizontal root mean square turbulent velocity u' (m/s), (b) vertical root mean square turbulent velocity v' (m/s), (c) turbulent kinetic energy k (m^2/s^2), and (d) Reynolds shear stress τ' (m^2/s^2). The dotted line is the ensemble-averaged free surface and the toe of the breaker is at $x/h_0 \sim 0.47$.

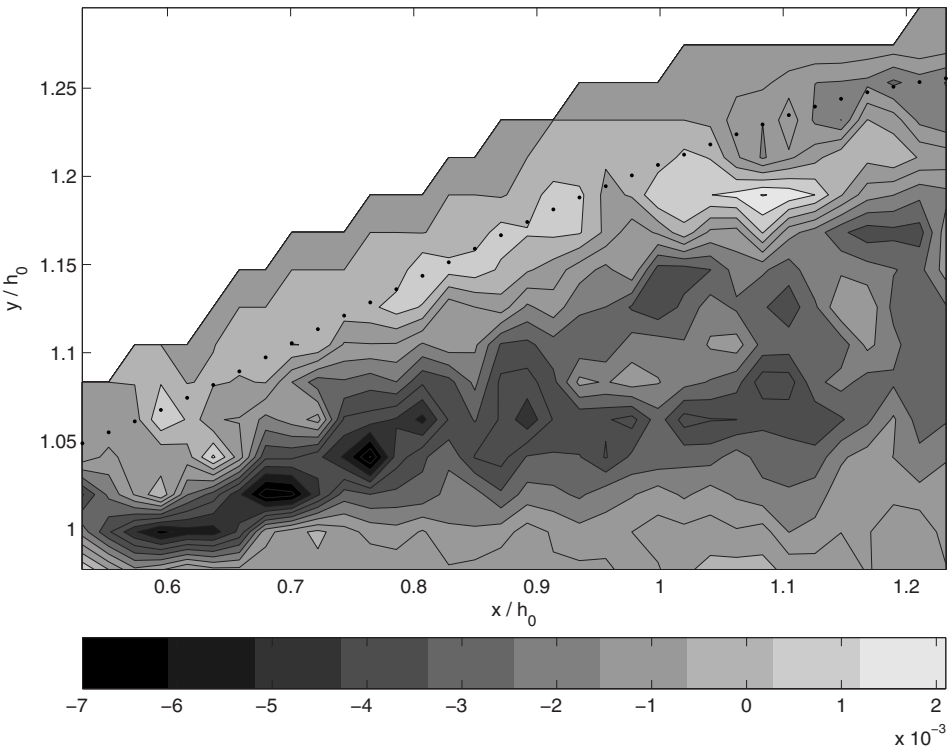

FIG. 19. Reynolds shear stress, τ' (m^2/s^2), in the reverse flow and breaker shear layer regions. The dotted line is the mean free surface.

noted the general similarity of the structure of the horizontal turbulence intensity (for their strongest jump, at Fr=3) with the present measurements. However, due to the undular characteristics, the location of the peak in u' in their case was downstream of the toe. In the present study, for the vertical turbulence velocity, the largest values occur at $\tilde{x}\sim 0.81$, $\tilde{y}\sim 1.04$ downstream of the toe of the breaker. The turbulent kinetic energy has its peak value at the toe of the breaker. This arises from the dominant contribution to k from the horizontal turbulence intensity. The Reynolds shear stress is negative throughout the shear layer, implying an upward diffusion of momentum. The Reynolds shear stress has its largest value at $\tilde{x}\sim 0.53$, $\tilde{y}\sim 1.02$, downstream of the toe and the location of the maximum negative mean simple shear $\partial U/\partial y$ which occurs at $\tilde{x}\sim 0.40$, $\tilde{y}\sim 0.98$, indicating that in addition to the simple shear, there are extra strain rates such as streamline curvature which affect the Reynolds stress structure (Bradshaw[60] and Misra *et al.*[61]). In the following section, we take a more detailed look at the Reynolds shear stress in the reverse-flow and breaker shear layer regions.

1. The reverse-flow region

Figure 19 shows that the Reynolds shear stress is positive about the mean surface indicating a downward flux of momentum from the reverse-flow region into the breaker shear layer. The magnitudes of the Reynolds stress are, on average, smaller than the breaker shear layer values. Further, the turbulent kinetic energy in the reverse-flow region is an order of magnitude smaller than in the shear layer suggesting that, even though in the intermittent region turbulent fluctuations are as important as the mean velocities, the turbulence intensity is much smaller than in the breaker shear layer as suggested by Peregrine and Svendsen.[17] The distribution of both horizontal and vertical turbulence intensities are qualitatively very similar to the turbulent kinetic energy distribution and decay monotonically away from the mean surface toward $\gamma=0$.

2. The breaker shear layer region

It is fairly well-established that there is an intense shear layer formed below a fully formed, spilling breaker which spreads downstream from the toe of the breaker. The dynamics of the breaker shear layer are different from those of a typical shear layer in several respects. The outer boundary of the breaker shear layer is marked by a turbulent interface with a strong density difference between air on one side and water on the other. The localized effects of an adverse pressure gradient and streamline curvature along with the unsteadiness of the external flow also modify the flow structure. There is still so little knowledge of the detailed turbulence structure of spilling breakers that it is a meaningful pursuit to search for similarities with well known turbulent flows and use established results as a starting point for a more detailed understanding and modeling of the complicated processes accompanying breaking. Although the concept of a mixing layer has been assumed in theoretical models for breakers (Svendsen and Madsen,[22] Cointe and Tulin,[23] and Rhee and Stern[24]) there is no experimental evidence for the suggested classification of the shear layer in a fully formed breaker as a mixing layer.

In Fig. 19, we show the detailed structure of the Reynolds shear stress in the breaker shear layer. A robust classification of the comparative structure of two-dimensional plane wakes, jets, and mixing layers has been suggested by Tennekes and Lumley[62] by describing the typical downstream variation of U_s and l. U_s is defined as the scale for the

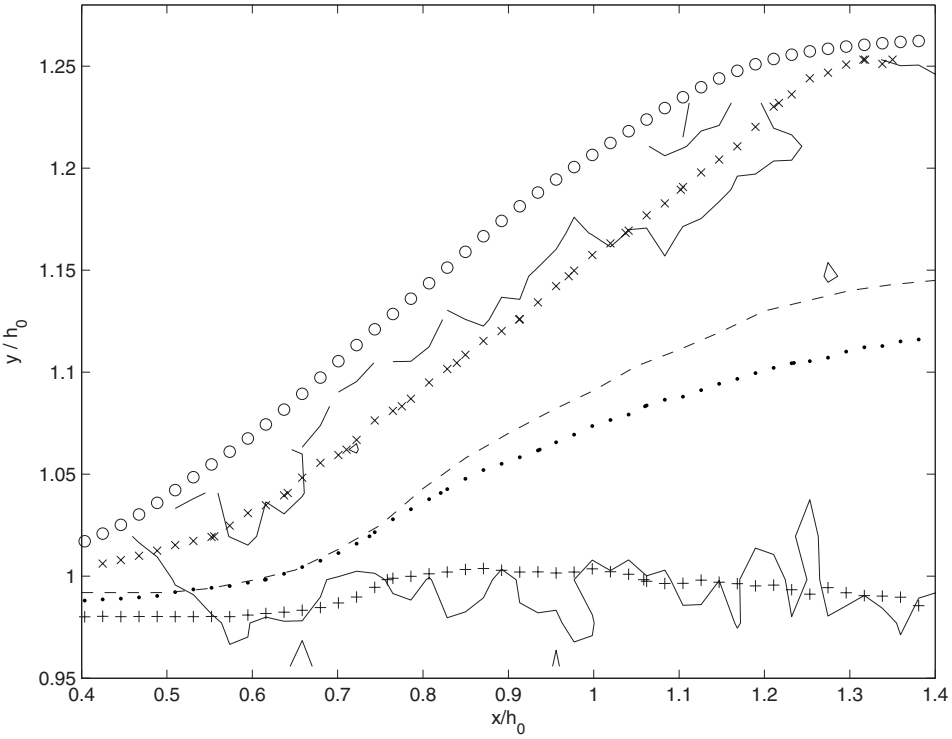

FIG. 20. Contours defined in the breaker shear layer region shown in the legend plot. See text for description.

cross-stream variation of the streamwise mean velocity component and for shear layers is equal to the maximum free-stream velocity. l is the cross-stream length scale defined as the distance from the center line to the location at which $(U-U_0)$ is equal to $1/2\,U_s$, where U_0 is the scale for the velocity of the mean flow in the streamwise direction. It is expected that for mixing layers, U_s is constant and l increases linearly with downstream distance. In turbulent mixing layers, the turbulent region is separated from the irrotational region by irregularly distorted bounding curves. In a practical sense, a finite percentage value of the maximum (magnitude) Reynolds shear stress in the region of interest has to be chosen to define the boundaries of the breaker shear layer. Due to the complicated turbulent structure seen in Fig. 19, we chose to define the boundaries at the location where the Reynolds shear stress decayed to 90% and 10% of its maximum value ($\tau'_{\max} \sim -0.0071\ \mathrm{m^2/s^2}$). These contours are shown as solid lines in Fig. 20. It was found that the mean streamwise velocity contours of 0.12 m/s and 0.73 m/s fit the τ' contours reasonably well, as shown in Fig. 20 by "cross" and "plus" signs, respectively. These values were approximately 10% of the maximum mean streamwise velocity in this region, and were chosen as U_0 and U_s, respectively. The constancy of U_s with downstream distance is, thus, automatically satisfied. The centerline of the layer was defined as the location of maximum shear, and is shown as the dashed line in Fig. 20. The velocity contour for $U_l \equiv U_0 + U_s/2 = 0.485$ m/s is shown as the dotted line. The length scale is calculated as the distance from this line to the centerline. The mean free surface is shown as circles.

In Brown and Roshko,[63] the virtual origin for the downstream coordinate is defined based on characteristic thicknesses calculated from their density and velocity profiles. The intersection of a linear fit to these thicknesses with the x-axis yielded the virtual origin. A similar approach was used by Battjes and Sakai[9] based on a linear fit to the calculated velocity defects. In the present case, a simpler visual approach is taken. By drawing tangents to the 10% contours of the Reynolds stress, we find that the location of their intersection is at $\tilde{x}_0 \sim 0.4$, upstream of the toe. This is a physically reasonable choice for the virtual origin, since the Reynolds shear stress reaches its characteristic value further downstream of this location.

The width of the shear layer, W, and the length scale are nondimensionalized by h_0 and are shown in Fig. 21 along with the linear least squares regression fits. The regression has been calculated using a 95% confidence interval and the R^2 statistical value (defined as the ratio of squares to total sum of squares) is also shown along with the estimated linear fit. Both fits are statistically accurate in representing the linear trend of the increase in the width and length scale of the breaker shear layer, as is evident from the high values of the R^2 estimate. This is in good qualitative agreement with the spreading rate of mixing layers where the "wedge" is known to spread in a linear fashion, and indicates that the breaker shear layer can be classified as a mixing layer with its origin downstream of the toe and extending downstream until it changes to a wake-type flow. This transition occurs at approximately the location of the peak negative curvature. The dimensionless length scale in the breaker shear layer is also shown in Fig. 21 and shows a linear increase from $\tilde{x} \sim 0.6$ until $\tilde{x} \sim 1.2$.

Another parameter of interest is the ratio $W/x-x_0$ referred to as the growth rate by Brown and Roshko.[63] In Brown and Roshko,[63] the linear fit to the data for a density ratio of unity is

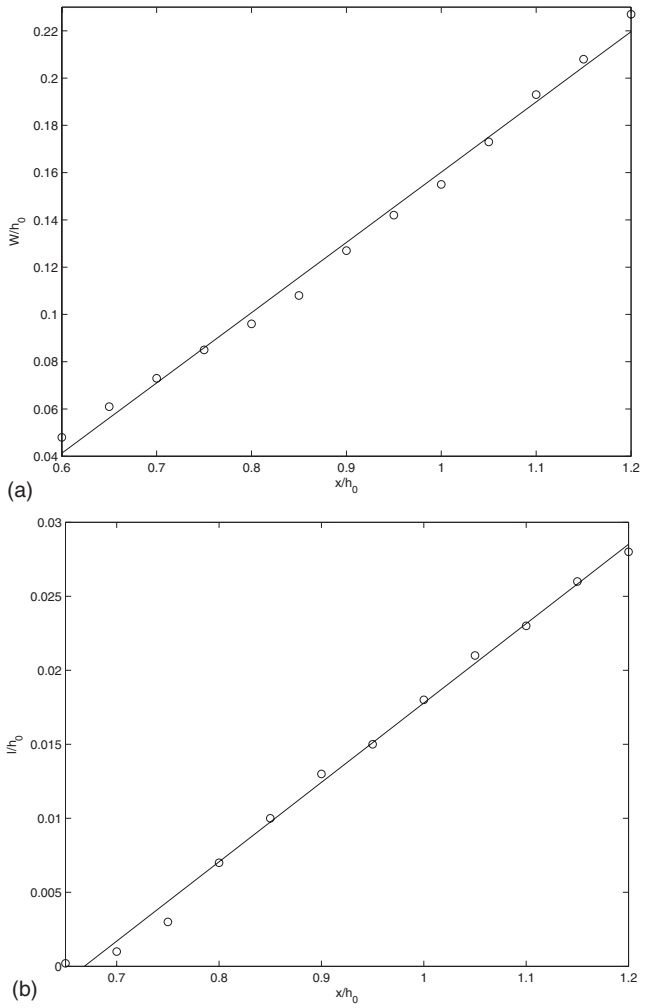

FIG. 21. (Top panel) Dimensionless width of the mixing layer W/h_0, best fit line given by $W/h_0=0.297x/h_0-0.137$ with $R^2=0.993$. (Bottom panel) Dimensionless length scale l/h_0, best fit line given by $l/h_0=0.0536x/h_0-0.0358$ with $R^2=0.9953$.

$$\frac{W}{x-x_0}=0.38\left[\frac{U_s-U_0}{U_s+U_0}\right]. \tag{12}$$

For $U_s-U_0/U_s+U_0=0.72$ (U_s and U_0, here, are taken equivalent to U_1 and U_2 in their case), this gives $W/x-x_0=0.27$. This is in good agreement with the mean value (averaged over the values from $\tilde{x}\sim 0.6$ to $\tilde{x}\sim 1.2$) for the growth rate in the present case, equal to 0.26.

F. Index of entrainment

For free turbulent flows, the ratio of standard deviation to the mean value of the interface fluctuations $[R=\sigma(\eta)/\eta_0]$ is a measure of relative depths of the corrugations of the bounding surface and in conjunction with the intensity of the interface vortices gives a measure of the activity of the entrainment at the interface (Townsend[64]). R is known to vary considerably depending on the turbulent flow regime, and since the definition of η_0 is dependent on the choice of the datum, it is first necessary to choose an appropriate length scale characterizing the surface fluctuations. We take the width of the intermittent region (where γ varies from 0 to 1) as η_0. The calculated entrainment ratio index is shown in Fig. 22(b) and is seen to vary between 0.15 and 0.27 in the breaking region. This is comparable to the values reported by Townsend[64] (see Table 6.2) for boundary layers (0.17), jets (0.22), and wakes (0.38). The entrainment index is seen to increase into the breaking breaker region where it stays approximately constant and then decreases further downstream. This gives a good qualitative insight into the variation of the intensity of the surface turbulence of the flow. Previous results of the intensity of surface turbulence for steady breaking waves found by Duncan and Dimas[65] and Walker *et al.*[58] agree with the trends observed above.

An important factor influencing the entrainment index is the intense shear generated at the toe of the breaker shear layer. A qualitative, and admittedly simplified, argument can be made for the trends observed in R by looking at the curvature of the ensemble-averaged surface shown in Fig. 7(c). A positive curvature implies concavity of the surface. The normal pressure gradient (with the positive normal being directed away from the surface) is, therefore, negative. This, in turn, implies an increase in entrainment downstream since a parcel of entrained fluid encounters a favorable pressure gradient. The situation is reversed for convexity when the curvature is negative, leading to a positive pressure gradient which opposes entrainment. In the presence of an adverse pressure gradient as in the present case, the influence of the curvature on the entrainment is reduced compared to a zero-pressure-gradient case, since the outer region streamlines are less curved than the surface (Simpson[66]). This might be the reason for the increase in entrainment taking place further upstream than the location of the peak positive curvature. Although the pressure was not directly measured, the mean pressure gradients can be calculated from the Cartesian momentum equations where it is assumed that $\partial U/\partial t\approx 0$, $\partial V/\partial t\approx 0$. The horizontal and vertical pressure gradients are thus calculated as

$$\frac{1}{\rho}\frac{\partial P}{\partial x}\approx -U\frac{\partial U}{\partial x}-V\frac{\partial U}{\partial y}-\frac{\partial}{\partial x}(\langle u'^2\rangle)-\frac{\partial}{\partial y}(\langle u'v'\rangle) \tag{13}$$

and

$$\frac{1}{\rho}\frac{\partial P}{\partial y}\approx -U\frac{\partial V}{\partial x}-V\frac{\partial V}{\partial y}-\frac{\partial}{\partial x}(\langle v'^2\rangle)-\frac{\partial}{\partial x}(\langle u'v'\rangle). \tag{14}$$

P is the ensemble-averaged pressure. The streamwise and surface-normal gradients are given by

$$\frac{\partial P}{\partial n}=-\sin(\theta)\frac{\partial P}{\partial x}+\cos(\theta)\frac{\partial P}{\partial y} \tag{15}$$

and

$$\frac{\partial P}{\partial s}=\cos(\theta)\frac{\partial P}{\partial x}+\sin(\theta)\frac{\partial P}{\partial y}. \tag{16}$$

As before, the results are shown only for five measurement locations below the mean surface. It can be seen from

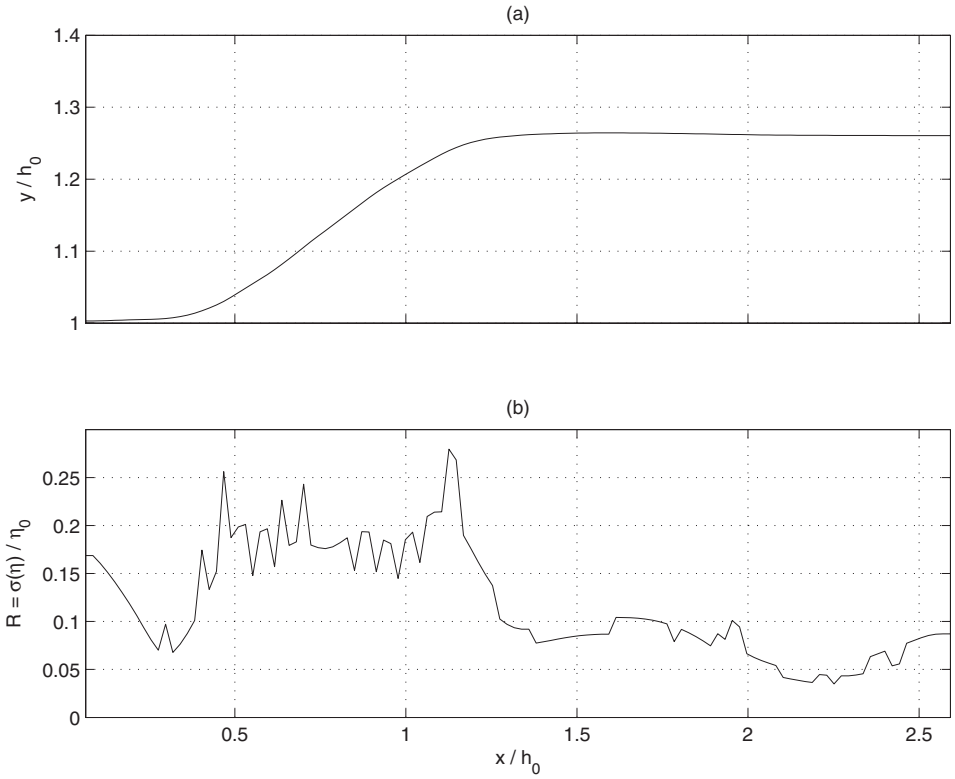

FIG. 22. (a) Ensemble-averaged free surface and (b) ratio of standard deviation to ensemble mean of the free surface, $R=\sigma(\eta)/\eta_0$. The toe of the breaker is at $x/h_0\sim 0.47$.

Fig. 23(b) that there is a strong adverse (positive) streamwise gradient of the specific pressure (per unit density) with its peak value located at $\tilde{x}\sim 0.47$, $\tilde{y}\sim 1.0$, i.e., at the toe of the breaker. This leads us to believe that the sharp curvature of the surface is induced by the flow separation which, in turn, is caused by the adverse pressure gradient. A short distance upstream of the peak value, the magnitude of the streamwise pressure gradient decreases drastically. This is typical of flows approaching separation and is attributed to the rapid thickening of the layer as a separation point is approached (Townsend[64]). The normal gradient has a negative peak at $\tilde{x}\sim 0.47$, $\tilde{y}\sim 0.98$. The highly anisotropic turbulence downstream of the toe of the breaker also contributes to a larger entrainment in the breaker shear layer.

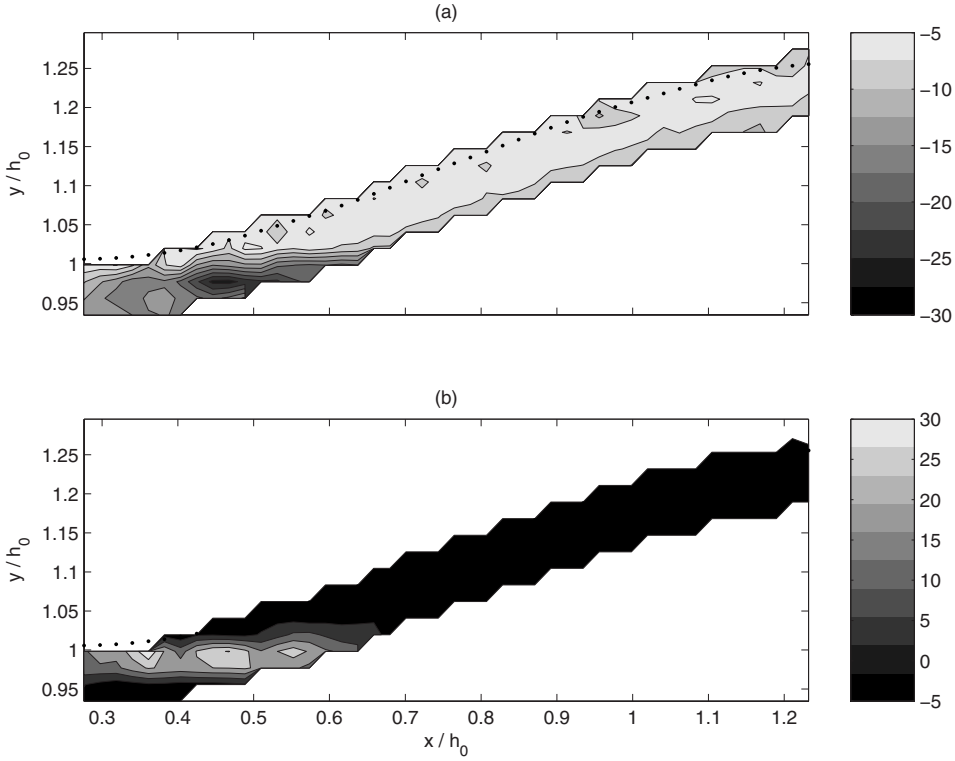

FIG. 23. (a) Surface-normal gradient of the specific pressure, $\partial P/\partial n$ $(\mathrm{m/s^2})$ and (b) surface-parallel gradient of the specific pressure $\partial P/\partial s$ $(\mathrm{m/s^2})$. The toe of the breaker is at $x/h_0\sim 0.47$.

V. CONCLUSIONS

PIV measurements of a weakly turbulent hydraulic jump of Fr=1.2 are analyzed in detail. An interface calculation method based on image segmentation was used to calculate the instantaneous free surface directly from the PIV images. This avoided the inclusion of spurious interface reflections. The turbulent surface fluctuations were seen to fit error function profiles well and give an indication of the entrainment index. In regions of upward surface curvature, a negative surface-normal pressure gradient leads to increased entrainment further downstream; the opposite occurs for regions with downward curvature.

The calculated velocity field is found to accurately satisfy mass conservation. An intense and thin shear layer originates near the toe of the breaker. The deceleration of the surface-parallel velocity has its largest (negative) value at the toe but large values are found at the peak vorticity location, which is slightly upstream of the toe location. The surface-parallel pressure gradient is highly localized and has its peak, positive value at the toe location. This leads us to believe that breaking for gravity-dominated waves is driven by a surface-parallel adverse pressure gradient and a streamwise flow deceleration, both occurring at the toe location. Both effects force the shear layer to thicken rapidly, inducing a sharp free surface curvature change at the toe. The mean shear is finite and negative at the mean surface. A weak reverse flow is found in the intermittent surface region. In this region, the mean surface-normal velocity was positive indicating entrainment of fluid from below. This is in good agreement with the "entraining plume" model of Longuet-Higgins and Turner.[57] The present topology of the reverse-flow region is different from the concept of an isolated recirculating eddy/"roller" bounded on the top by a mean surface and on the bottom by a dividing streamline as indicated by SVBK00, since there clearly is reverse flow above the mean surface. As noted by Banner and Phillips,[67] we believe it essential to replace the idea of a mean surface in the reverse-flow region by an intermittency zone.

The turbulent kinetic energy is maximum at the toe of the breaker and the Reynolds shear stress is positive just below the mean surface, signifying the downward transfer of momentum from the reverse-flow region, into the shear layer. The turbulence intensity in the intermittent surface region is an order of magnitude smaller than that in the breaker shear layer. In the shear layer, the Reynolds shear stress is negative, indicative of an upward diffusion of momentum from the nearly irrotational flow below. The structural similarity of the turbulence structure in the shear layer was compared to those of well-known plane shear flows. The breaker shear layer is seen to resemble a plane mixing layer; the width of the layer, and the length scale grow linearly with distance from the toe until they become constant around the location of the maximum downward curvature. The mean value of the nondimensional growth rate in the mixing layer is found to be in good agreement with values found earlier by Brown and Roshko.[63] A more robust quantification of the length scales can be obtained by an analysis of the coherent turbulent structures.

ACKNOWLEDGMENTS

S.K.M. and J.T.K. acknowledge the support of the National Oceanographic Partnership Program (NOPP) Grant No. N00014-99-1-1051. S.K.M. acknowledges Dr. R. Briganti's help with the spectra calculations, P. Teran Cobo's help with the ADVs, and stimulating discussions with F. D. Santos. This paper is dedicated to the memory of our esteemed colleague, Dr. Ib Arne Svendsen (1937–2004).

[1] H. Rouse, T. T. Siao, and S. Nagarathnam, "Turbulence characteristics of the hydraulic jumps," J. Highw. Div. **84**, 926 (1959).
[2] F. J. Resch and H. J. Leutheusser, "Reynolds stress measurements in hydraulic jumps," J. Hydraul. Res. **10**, 409 (1972).
[3] D. Long, P. M. Steffler, and N. Rajaratnam, "LDA structure of flow structure in submerged hydraulic jumps," J. Hydraul. Res. **4**, 437 (1990).
[4] M. Liu, N. Rajaratnam, and D. Z. Zhu, "Turbulence structure of hydraulic jumps of low Froude numbers," J. Hydraul. Eng. **130**, 511 (2004).
[5] B. S. Hyun, R. Balachander, K. Yu, and V. C. Patel, "Assessment of PIV to measure mean velocity and turbulence in open-channel flow," Exp. Fluids **35**, 262 (2003).
[6] H. G. Hornung, C. Willert, and S. Turner, "The flow field of a hydraulic jump," J. Fluid Mech. **287**, 299 (1995).
[7] J. M. Lennon and D. F. Hill, "Particle image velocimetry measurements of hydraulic and undular jumps," J. Hydraul. Eng. **132**, 1283 (2005).
[8] J. H. Duncan, "An experimental investigation of breaking waves produced by a towed hydrofoil," Proc. R. Soc. London, Ser. A **377**, 331 (1981).
[9] J. A. Battjes and T. Sakai, "Velocity field in a steady breaker," J. Fluid Mech. **111**, 421 (1981).
[10] J. H. Duncan, "The breaking and non-breaking wave resistance of a two-dimensional hydrofoil," J. Fluid Mech. **126**, 507 (1983).
[11] M. L. Banner, "Surging characteristics of spilling zones of quasi-steady breaking water waves," in *Nonlinear Water Waves*, International Union of Theoretical and Applied Mechanics Symposium, edited by K. Horikawa and H. Maruo (Springer-Verlag, Germany, 1988), pp. 151–158.
[12] E. B. Thornton and R. T. Guza, "Transformation of wave height distribution," J. Geophys. Res. **88**, 5925, DOI: 10.1029/JC088iC10p05925 (1983).
[13] F. C. K. Ting, "Wave and turbulence characteristics in narrow-banded irregular breaking waves," Coastal Eng. **46**, 291 (2002).
[14] J. A. Battjes, "Surf-zone dynamics," Annu. Rev. Fluid Mech. **111**, 257 (1981).
[15] I. A. Svendsen, J. Veeramony, J. Bakunin, and J. T. Kirby, "The flow in weak turbulent hydraulic jumps," J. Fluid Mech. **418**, 25 (2000).
[16] J. Bakunin, "Experimental Study of Hydraulic Jumps in Low Froude Number Range," M.S. thesis, Department of Civil and Environmental Engineering, University of Delaware (1995).
[17] D. H. Peregrine and I. A. Svendsen, "Spilling breakers, bores and hydraulic jumps," in *Proceedings of the 16th International Conference on Coastal Engineering* (ASCE, Hamburg, 1978), pp. 540–555.
[18] J. W. Hoyt and R. H. J. Sellin, "Hydraulic jump as 'mixing layer'," J. Hydraul. Eng. **115**, 1607 (1989).
[19] N. Rajaratnam, "The hydraulic jump as a wall jet," J. Hydr. Div. **91**, 107 (1965).
[20] R. Narayanan, "Wall jet analogy to hydaulic jump," J. Hydr. Div. **101**, 347 (1975).
[21] H. Chanson and T. Brattberg, "Experimental study of the air-water shear flow in a hydraulic jump," Int. J. Multiphase Flow **26**, 583 (2000).
[22] I. A. Svendsen and P. A. Madsen, "A turbulent bore on a beach," J. Fluid Mech. **148**, 73 (1984).
[23] R. Cointe and M. P. Tulin, "A theory of steady breakers," J. Fluid Mech. **276**, 1 (1994).
[24] S. H. Rhee and F. Stern, "RANS model for spilling breaking waves," J. Fluids Eng. **124**, 424 (2002).
[25] F. M. Henderson, *Open Channel Flow* (MacMillan, New York, 1970).
[26] V. T. Chow, *Open Channel Hydraulics* (McGraw-Hill, New York, 1959).
[27] M. R. Maxey, "The gravitational settling of aerosol particles in homogenous turbulence and random flow fields," J. Fluid Mech. **174**, 441 (1987).
[28] Q. Wang, K. D. Squires, and L. Wang, "On the effect of nonuniform seeding on particle dispersion in two-dimensional mixing layers," Phys. Fluids **10**, 1700 (1998).

[29]Y. A. Hassan, K. Okamoto, and O. G. Philip, "Investigation of the interaction between a fluid flow and the fluid's free surface using particle image velocimetry," in *9th International Symposium on Transport Phenomena in Thermal-Fluids Engineering* edited by S. H. Winoto, Y. T. Chew, and N. E. Wijeysundera (1996), pp. 566–574.
[30]W. L. Peirson, "Measurement of surface velocities and shear at a wavy air-water interface using particle image velocimetry," Exp. Fluids **23**, 427 (1997).
[31]C. N. S. Law, B. C. Khoo, and T. C. Chen, "Turbulence structure in the immediate vicinity of the shear-free air-water interface induced by a deeply submerged jet," Exp. Fluids **27**, 321 (1999).
[32]H. J. Lin and M. Perlin, "Improved methods for thin, surface boundary layer investigations," Exp. Fluids **25**, 431 (1998).
[33]L. Tsuei and T. Savaş, "Treatment of interfaces in particle image velocimetry," Exp. Fluids **29**, 203 (2000).
[34]S. K. Misra, M. Thomas, C. Kambhamettu, J. T. Kirby, F. Veron, and M. Brocchini, "Estimation of complex air-water interfaces from PIV images," Exp. Fluids **40**, 764 (2005).
[35]F. Veron, G. Saxena, and S. K. Misra, "Measurements of the viscous tangential stress in the airflow above wind waves," Geophys. Res. Lett. **34**, L05402, DOI: 10.1029/2006GL029147 (2007).
[36]H. Chanson, *Air Bubble Entrainment in Free-Surface Turbulent Shear Flows* (Academic, New York, 1996).
[37]H. Chanson and J. S. Montes, "Characteristics of undular hydraulic jumps. Experimental apparatus and flow patterns," J. Hydraul. Eng. **121**, 129 (1995).
[38]J. H. Duncan, "Spilling breakers," Annu. Rev. Fluid Mech. **33**, 519 (2001).
[39]H. Qiao and J. H. Duncan, "Gentle spilling breakers: Crest flow-field evolution," J. Fluid Mech. **439**, 57 (2001).
[40]M. S. Longuet-Higgins, "Shear instability in spilling breakers," Proc. R. Soc. London, Ser. A **446**, 399 (1994).
[41]J. H. Duncan, H. Qiao, V. Philomin, and A. Wenz, "Gentle spilling breakers: Crest profile evolution," J. Fluid Mech. **379**, 191 (1999).
[42]M. Brocchini and D. H. Peregrine, "The dynamics of strong turbulence at free surfaces. Part 2. Free-surface boundary conditions," J. Fluid Mech. **449**, 255 (2001).
[43]D. Dabiri and M. Gharib, "Experimental investigation of the vorticity generation within a spilling water wave," J. Fluid Mech. **330**, 113 (1997).
[44]J. C. Lin and D. Rockwell, "Evolution of a quasisteady breaking wave," J. Fluid Mech. **302**, 29 (1995).
[45]H. A. Schaffer, P. A. Madsen, and R. Deigaard, "A Boussinesq model for waves breaking in shallow water," Coastal Eng. **20**, 185 (1993).
[46]R. Briganti, R. E. Musumeci, G. Bellotti, M. Brocchini, and E. Foti, "Boussinesq modeling of breaking waves: Description of turbulence," J. Geophys. Res. **109**, C07015, DOI: 10.1029/2003JC002065 (2004).
[47]N. Salvesen and C. von Kerczek, "Nonlinear aspects of free-surface flow past two-dimensional bodies," in *14th International Union of Theoretical and Applied Mechanics Delft* (Springer-Verlag, Germany, 1976).
[48]M. S. Longuet-Higgins, "A model of flow separation at a free surface," J. Fluid Mech. **57**, 129 (1973).
[49]R. A. Antonia, "Conditional sampling in turbulent measurement," Annu. Rev. Fluid Mech. **13**, 131 (1981).
[50]S. Corrsin and A. L. Kistler, "Free-stream boundaries of turbulent flows," National Advisory Committee for Aeronautics, Washington, Report No. 1244 (1955), p. 1244, available at htpp://naca.central.cranfield.ac.uk/reports/1955/naca-report-1244.pdf.
[51]J. M. Killen and A. G. Anderson, "A study of the air-water interface in air-entrained flow in open channels," in *Proceedings of the 13th International Association of Hydrautic Engineering and Research Congress*, Kyoto, Japan (1969).
[52]D. A. Ervine and H. T. Falvey, "Behavior of turbulent water jets in the atmosphere and in plunge pools," in *Proceedings of the Institute of Civil Engineering* (Thomas Telford, London, 1987), Part 2, Vol. 83, pp. 295–314.
[53]M. Brocchini and D. H. Peregrine, "Integral flow properties of the swash zone and averaging," J. Fluid Mech. **317**, 241 (1996).
[54]M. Thomas, S. K. Misra, C. Kambhamettu, and J. T. Kirby, "A robust motion estimation algorithm for PIV," Meas. Sci. Technol. **16**, 865 (2005).
[55]J. Nogueira, A. Lecuona, and P. A. Rodriguez, "Limits on the resolution of correlation PIV iterative methods. Fundamentals," Exp. Fluids **39**, 305 (2005).
[56]E. H. Wilson and A. A. Turner, "Boundary layer effects on hydraulic jump location," J. Hydr. Div. **98**, 1127 (1972).
[57]M. S. Longuet-Higgins and J. S. Turner, "An 'entraining plume' model of a spilling breaker," J. Fluid Mech. **63**, 1 (1974).
[58]D. T. Walker, D. R. Lyzenga, E. A. Ericson, and D. E. Lund, "Radar backscatter and surface roughness measurements for stationary breaking waves," Proc. R. Soc. London, Ser. A **452**, 1953 (1996).
[59]U. Ullum, J. J. Schmidt, P. S. Larsen, and D. R. McCluskey, "Statistical analysis and accuracy of PIV data," J. Visualization **1**, 205 (1998).
[60]P. Bradshaw, "Effects of streamline curvature on turbulent flow," AGARDograph, Vol. 169 (1973).
[61]S. K. Misra, J. T. Kirby, M. Brocchini, M. Thomas, F. Veron, and C. Kambhamettu, "Extra strain rates in spilling breaking waves," in *Proceedings of the 29th International Conference on Coastal Engineering, Lisbon* (ASCE, Reston, Virginia, 2004). pp. 370–378.
[62]H. Tennekes and J. L. Lumley, *A First Course in Turbulence* (MIT, Cambridge, 1972).
[63]G. L. Brown and A. Roshko, "On density effects and large structures in turbulent mixing layers," J. Fluid Mech. **64**, 775 (1974).
[64]A. A. Townsend, *The Structure of Turbulent Shear Flow*, 2nd ed. (Cambridge University Press, Cambridge, 1976).
[65]J. H. Duncan and A. Dimas, "Surface ripples due to steady breaking waves," J. Fluid Mech. **329**, 309 (1996).
[66]R. L. Simpson, "Turbulent boundary layer separation," Annu. Rev. Fluid Mech. **21**, 205 (1989).
[67]M. L. Banner and O. M. Phillips, "On the incipient breaking of small scale waves," J. Fluid Mech. **65**, 647 (1974).